

## **Title**

Robust frequency-dependent diffusion kurtosis computation using an efficient direction scheme, axisymmetric modelling, and spatial regularization

## **Authors & Affiliations**

Jake Hamilton<sup>1,2</sup>, Kathy Xu<sup>3,4</sup>, Arthur Brown<sup>3,4</sup>, Corey A. Baron<sup>1,2</sup>

1. Centre for Functional and Metabolic Mapping (CFMM), Robarts Research Institute, University of Western Ontario, London, Ontario, Canada

2. Department of Medical Biophysics, Schulich School of Medicine and Dentistry, University of Western Ontario, London, Ontario, Canada

3. Translational Neuroscience Group, Robarts Research Institute, Schulich School of Medicine and Dentistry, University of Western Ontario, London, Ontario, Canada

4. Department of Anatomy and Cell Biology, University of Western Ontario, London, Ontario, Canada

**Corresponding author:** Corey A. Baron (corey.baron@uwo.ca)

Submitted to Imaging Neuroscience

## **Abstract**

Frequency-dependent diffusion MRI (dMRI) using oscillating gradient encoding and diffusion kurtosis imaging (DKI) techniques have been shown to provide additional insight into tissue microstructure compared to conventional dMRI. However, a technical challenge when combining these techniques is that the generation of the large b-values required for DKI is difficult when using oscillating gradient diffusion encoding. While efficient encoding schemes can enable larger b-values by maximizing multiple gradient channels simultaneously, they do not have sufficient directions to enable fitting of the full kurtosis tensor. Accordingly, we investigate a DKI fitting algorithm that combines axisymmetric DKI fitting, a prior that enforces the same axis of symmetry for all oscillating gradient frequencies, and spatial regularization, which together enable robust DKI fitting for a 10-direction scheme that offers double the b-value compared to traditional direction schemes. Using data from mice (oscillating frequencies of 0, 60, and 120 Hz) and humans (0 Hz only), we first show that axisymmetric modelling is advantageous over full kurtosis tensor fitting in terms of preserving contrast and reducing noise in DKI maps, and improved DKI map quality when using an efficient encoding scheme with averaging as compared to a traditional scheme with more encoding directions. We also demonstrate how spatial regularization during fitting preserves spatial features better than using Gaussian filtering prior to fitting, which is an oft-reported preprocessing step for DKI, and that enforcing consistent axes of symmetries across frequencies improves fitting quality. Thus, the use of an efficient 10-direction scheme combined with the proposed DKI fitting algorithm provides robust maps of frequency-dependent directional kurtosis parameters that can be used to explore novel biomarkers for various pathologies.

**Keywords:** Diffusion MRI, Diffusion kurtosis, Oscillating gradient, Spatial regularization, Diffusion dispersion

## 1. Introduction

1 Diffusion MRI (dMRI) is a well-known technique that allows probing of tissue microstructure on  
2 spatial scales unattainable with conventional MRI techniques. Diffusion kurtosis imaging (DKI) is  
3 a form of dMRI that quantifies the non-Gaussian component of diffusion within tissue,  
4 providing greater sensitivity to microstructural changes as compared to conventional diffusion  
5 tensor imaging (DTI) (Jensen et al., 2005; Jensen & Helpert, 2010). DKI has been used to study  
6 various pathologies such as stroke (Grinberg et al., 2012; Lampinen et al., 2021), mild traumatic  
7 brain injury (Stenberg et al., 2021; Stokum et al., 2015), neurodegenerative diseases (Chu et al.,  
8 2022; Dong et al., 2020; Falangola et al., 2013; Vanhoutte et al., 2013), as well as many others  
9 (Steven et al., 2014), and has shown increased sensitivity to changes in tissue microstructure  
10 than DTI. An important sequence parameter to consider when interpreting changes in dMRI  
11 metrics is the effective diffusion time ( $\Delta t_{\text{eff}}$ ) which determines the length scale within the tissue  
12 being probed. Commonly used pulsed gradient spin echo (PGSE) sequences to encode diffusion  
13 are limited to relatively long  $\Delta t_{\text{eff}}$  ( $> 10$  ms) for typical pre-clinical gradient hardware (Jelescu et  
14 al., 2022; Portnoy et al., 2013), meaning the acquired signal reflects diffusion restriction at  
15 multiple spatial scales (i.e., both cellular and sub-cellular). Conversely, encoding diffusion using  
16 an oscillating gradient spin echo (OGSE) sequence allows much shorter  $\Delta t_{\text{eff}}$  (corresponding to  
17 higher OGSE frequencies), increasing sensitivity to smaller spatial scales (Schachter et al., 2000).  
18 By collecting data at multiple gradient oscillation frequencies (i.e., frequency-dependent dMRI),  
19 the spatial scale sensitivity can be varied, enabling investigation of tissue microstructure at both  
20 sub-cellular and cellular levels, increasing sensitivity and specificity for studying various  
21 pathological conditions. Exploiting the frequency-dependence of DTI metrics has been well-  
22 characterized in the healthy brain (Baron & Beaulieu, 2014), as well as in the study of stroke  
23 (Baron et al., 2015), cancer (Iima et al., 2019; Maekawa et al., 2020), and in neurodegenerative  
24 disease (Aggarwal et al., 2014). Conversely, the dependence of DKI metrics on OGSE frequency  
25 is less understood but has been characterized in healthy humans (Dai et al., 2023) and rodents  
26 (Aggarwal et al., 2020; Pyatigorskaya et al., 2014), as well as in rodent studies of hypoxic-  
27 ischemic injury (Wu et al., 2018) and a demyelination disease model (Aggarwal et al., 2020).

28 A key technical challenge in using frequency-dependent DKI is that OGSE sequences are much  
29 less efficient at generating the large b-values required for DKI compared to PGSE, as b-value is  
30 related to the gradient strength (G) and OGSE frequency (f) through  $b \sim G^2 / f^3$  (Xu, 2021).  
31 Consequently, tetrahedral (4 directions) encoding schemes (Conturo et al., 1999) have been  
32 required in humans (Borsos et al., 2023) and mice (Aggarwal et al., 2020) to generate the  
33 desired b-value for diffusion kurtosis fitting. However, this direction scheme does not allow for  
34 directional parameters to be calculated and likely introduces rotational variance in computed  
35 metrics (Jones, 2004; Nilsson et al., 2020). Directional (axial and radial) kurtosis parameters  
36 have been shown to provide additional specificity to changes in mean kurtosis (Conklin et al.,  
37 2016; Goryawala et al., 2018), but estimation of the full kurtosis tensor requires at least two  
38 non-zero b-value shells with 15 independent diffusion directions (Lu et al., 2006). A recently  
39 developed fitting method, axisymmetric DKI (Hansen et al., 2016), allows fitting of directional  
40 kurtosis parameters with two non-zero b-value shells and 9 independent diffusion directions.  
41 This method requires determination of a symmetric axis of diffusion within each voxel to which  
42 kurtosis parameters are fit to based on the relation between encoding direction and the  
43 symmetric axis. This method has been shown to generate comparable and even improved  
44 kurtosis maps to those computed via kurtosis tensor fitting (Hansen et al., 2016; Jespersen,  
45 2018; Oeschger et al., 2023).

46 A second challenge when using DKI is noise propagation, primarily due to the high diffusion-  
47 weighting that is required to compute kurtosis in addition to the large number of parameters to  
48 be fit when estimating the kurtosis tensor (i.e., noise amplification) (Glenn et al., 2015; Tabesh  
49 et al., 2011). Subsequently, Gaussian smoothing on diffusion-weighted images prior to fitting is  
50 widely accepted as a necessary pre-processing step used to reduce noise levels in kurtosis maps  
51 (Jensen et al., 2005; Tax et al., 2022). However, because there is averaging of signal from  
52 neighboring voxels, this leads to blurring around sharp edges within the image and can cause  
53 bias in quantitative analysis (Falconer & Narayana, 1997; Pfefferbaum & Sullivan, 2003; Vos et  
54 al., 2011). An alternative approach is to use spatial regularization (Tikhonov et al., 1995) during  
55 fitting which balances smoothing of noise with the fitting residual. Regularization has been

56 shown to be advantageous over Gaussian smoothing in functional MRI studies in terms of  
57 retaining original image contrast and detection of true areas of activation (Casanova et al.,  
58 2009; Liu et al., 2010; Ou & Golland, 2005). It has also been used to control noise amplification  
59 in various avenues of dMRI (McGraw et al., 2009; Veraart et al., 2016; Wu & Yan, 2021),  
60 however, its use during DKI fitting remains underutilized.

61 In this study we aim to delineate an acquisition and analysis scheme capable of generating high  
62 quality frequency-dependent kurtosis maps. We present a 10-direction scheme that is two  
63 times more efficient in generating b-value compared to traditional schemes, mitigating a key  
64 technical challenge when combining OGSE and DKI techniques. Further, we propose that using  
65 data from all frequencies and b-values to estimate the symmetric axis of diffusion will provide a  
66 more robust estimate that will reduce noise in parameter maps. We then introduce a two-step  
67 spatial regularization algorithm to reduce noise both during symmetric axis determination and  
68 kurtosis fitting. We also provide direct comparison demonstrating the advantage of collapsing  
69 data from all frequencies to determine the axis of symmetry and using this regularization  
70 algorithm over conventional Gaussian smoothing.

## 2. Methods

### 2.1. Human connectome project (HCP) data

71 Pre-processed dMRI data of a healthy female subject from the HCP1200 release of the Human  
72 Connectome Project (HCP) (McNab et al., 2013; Sotiropoulos et al., 2013) was used for  
73 validation of axisymmetric DKI fitting and spatial regularization. dMRI data was acquired on a 3  
74 Tesla (T) scanner with parameters:  $1.25 \times 1.25 \times 1.25 \text{ mm}^3$  voxel size, TE/TR = 89.5/5520 ms.  
75 Data consisted of 18  $b=0$  images and 3 b-value shells of 1000, 2000, and 3000  $\text{s/mm}^2$ , with 90  
76 directions at each. Data from the highest b-value shell (3000  $\text{s/mm}^2$ ) was excluded as the  
77 kurtosis fit is known to be most robust at b-values  $\leq 2500 \text{ s/mm}^2$  (Jelescu et al., 2022; Kiselev &  
78 Il'yasov, 2007). Full details regarding data acquisition can be found in the HCP 1200 subjects

79 reference manual (<https://www.humanconnectome.org/study/hcp-young->  
80 [adult/document/1200-subjects-data-release](https://www.humanconnectome.org/study/hcp-young-adult/document/1200-subjects-data-release)).

## 2.2. Subject info

81 Data was collected from 8 transgenic mice (4 males) with humanized *mapt* and *app* genes  
82 knock in at 6 months of age as part of another ongoing study, and one female mouse of the  
83 same genotype and age to compare our efficient direction scheme with a traditional scheme.  
84 All animal procedures were approved by the University of Western Ontario Animal Care  
85 Committee and were consistent with guidelines established by the Canadian Council on Animal  
86 Care. Before scanning sessions, anesthesia was induced by placing mice in an induction  
87 chamber with 4% isoflurane and an oxygen flow rate of 1.5 L/min. Throughout the scanning  
88 session, isoflurane was maintained at 1.8% with an oxygen flow rate of 1.5 L/min through a  
89 custom-built nose cone.

## 2.3. Data acquisition & pre-processing

90 In vivo MR scanning sessions were performed on a 9.4 T Bruker small animal scanner equipped  
91 with a gradient coil insert of 1 T/m strength (slew rate = 4,000 T/m/s). Both anatomical and  
92 diffusion scans were acquired for each subject. Anatomical images were acquired using a T2-  
93 weighted TurboRARE sequence with parameters: in-plane resolution 100 x 100  $\mu\text{m}^2$ , slice  
94 thickness 500  $\mu\text{m}$ , TE/TR = 30/5500 ms, 24 averages, scan time of 25 minutes. The dMRI  
95 protocol included a PGSE sequence (gradient duration = 9.4 ms and diffusion time = 12.4 ms)  
96 and OGSE sequences with frequencies of 60 and 120 Hz (corresponding  $\Delta t_{\text{eff}}$  of 4.2 and 2.1 ms  
97 (Does et al., 2003)). The lowest OGSE frequency (60 Hz) implements the recently introduced  
98 frequency tuned bipolar waveforms to reduce the TE of the acquisition (Borsos et al., 2023). For  
99 all frequencies, data consisted of 2  $b = 0$  images and two b-value shells of 1000 and 2500  $\text{s}/\text{mm}^2$   
100 each with the 10-direction scheme outlined in Table 1. This scheme is an efficient 6-direction  
101 scheme (Baron & Beaulieu, 2014) combined with a tetrahedral scheme (Aggarwal et al., 2020;  
102 Borsos et al., 2023), which offers a factor of 2 larger b-value than typical schemes due to at

103 least two gradient channels being simultaneously at maximum for each direction. The dMRI  
 104 protocol was acquired in one integrated scan using single-shot echo planar imaging with 80% of  
 105 k-space being sampled in the phase encode direction and parameters: in-plane resolution 200 x  
 106 200  $\mu\text{m}^2$ , slice thickness 500  $\mu\text{m}$ , TE/TR = 35.5/15000 ms, 4 averages, total scan time of 66  
 107 minutes. To compare our direction scheme with a traditional scheme, two diffusion protocols  
 108 were acquired during a single scanning session in one mouse. Both protocols had the same scan  
 109 time of 66 minutes and OGSE frequencies of 0, 60, and 120 Hz. The first protocol was the same  
 110 as described above: TE/TR = 35.5/15000 ms, 10 directions (Table 1), 4 averages, 4 b=0 images,  
 111 and the second (traditional) protocol with parameters: TE/TR = 52/15000 ms, 40 directions  
 112 isotropically distributed using electrostatic repulsion (Jones et al., 1999), 1 average, 4 b=0  
 113 images. Note the much longer TE required for the 2<sup>nd</sup> protocol in order to achieve the same b-  
 114 value with the less efficient direction scheme. For all acquisitions, complex-valued averages  
 115 were combined using in-house MATLAB code which included partial Fourier reconstruction,  
 116 phase alignment, frequency and signal drift correction, and Marchenko-Pastur denoising  
 117 (Veraart et al., 2016), similar to earlier work (Rahman et al., 2021). Data then underwent Gibbs  
 118 ringing correction using MRtrix3 (Tournier et al., 2019) followed by EDDY (Andersson &  
 119 Sotiropoulos, 2016) from FMRIB Software Library (FSL, Oxford, UK) (Smith et al., 2004) to  
 120 correct for eddy current induced distortions.  
 121

<b>x</b>	<b>y</b>	<b>z</b>
0	1	1
0	1	-1
1	0	1
1	0	-1
1	1	0
1	-1	0
$\sqrt{2/3}$	$\sqrt{2/3}$	$\sqrt{2/3}$
$\sqrt{2/3}$	$\sqrt{2/3}$	$-\sqrt{2/3}$
$\sqrt{2/3}$	$-\sqrt{2/3}$	$\sqrt{2/3}$
$-\sqrt{2/3}$	$\sqrt{2/3}$	$\sqrt{2/3}$

**Table 1.** The 10-direction scheme.

## 2.4. Data fitting

### 2.4.1. Axisymmetric DKI

122 The representation of the diffusion-weighted signal in DKI is given by (Jensen et al., 2005):

$$\log\left(\frac{S_{b,\hat{n}}}{S_0}\right) = -bD_{\hat{n}} + \frac{b^2}{6}\bar{D}^2W_{\hat{n}} \quad (1)$$

123 where  $S_{b,\hat{n}}$  is the diffusion-weighted signal at a particular diffusion weighting,  $b$ , and encoding  
124 direction  $\hat{n}$ ,  $S_0$  is the signal intensity at  $b=0$ ,  $D$  is the diffusion tensor, and  $W$  is the kurtosis  
125 tensor. As outlined by Hansen et al. (2016), in systems assumed to have axial symmetry (i.e., in  
126 the diffusion tensor,  $\lambda_2 = \lambda_3$ ), kurtosis is characterized by three independent parameters:  
127 mean kurtosis ( $\bar{W}$ ), radial kurtosis ( $K_{\perp}$ ), and axial kurtosis ( $K_{\parallel}$ ). In such a system, the elements  
128 of  $W$  and  $D$  measured along any diffusion direction are given by:

$$W(\theta) = \frac{1}{16}(\cos(4\theta)(10W_{\perp} + 5W_{\parallel} - 15\bar{W}) + 8\cos(2\theta)(W_{\parallel} - W_{\perp}) - 2W_{\perp} + 3W_{\parallel} + 15\bar{W}) \quad (2)$$

and

$$D(\theta) = D_{\perp} + \cos^2(\theta)(D_{\parallel} - D_{\perp}) \quad (3)$$

129 where  $\theta$  is the polar angle between the axis of symmetry and the diffusion encoding direction,  
130  $D_{\perp}$  is the radial diffusivity, and  $D_{\parallel}$  is the axial diffusivity. Subsequently, mean diffusivity ( $\bar{D}$ ),  
131 fractional anisotropy (FA),  $K_{\parallel}$  and  $K_{\perp}$  can be calculated as:

$$\bar{D} = \frac{2D_{\perp}}{3} + \frac{D_{\parallel}}{3} \quad FA = \sqrt{\frac{3(D_{\parallel} - \bar{D})^2 + 2(D_{\perp} - \bar{D})^2}{D_{\parallel}^2 + 2D_{\perp}^2}} \quad K_{\parallel} = \frac{W_{\parallel}^2 \cdot \bar{D}^2}{D_{\parallel}^2} \quad K_{\perp} = \frac{W_{\perp}^2 \cdot \bar{D}^2}{D_{\perp}^2} \quad (4,5,6,7)$$



### 2.4.2. Spatial regularization

132 For maps with spatial regularization, a two-step algorithm was used to: (1) provide a robust  
 133 estimate of the symmetric axis in each voxel, and (2) reduce noise amplification in parameter  
 134 maps during the fitting process. Regularization was implemented using the conjugate gradient  
 135 method (Ginsburg, 1963), solved with ordinary least squares optimization. Ordinary least  
 136 squares was chosen for all optimizations as this method is known to have reduced bias relative  
 137 to weighted least squares (Morez et al., 2023).

138 *Step One:* In the first step, fitting of the diffusion tensor was regularized for the purpose of  
 139 determining the axis of symmetry within each voxel, using isotropic total variation (Rudin et al.,  
 140 1992), where  $\gamma_{DT}$  controls the strength of regularization:

$$\operatorname{argmin} \|A_{DTI}x_{DT} - y\|_2^2 + \gamma_{DT} \|T_{DT}x_{DT}\|_2^2 \quad (8)$$

141 The data consistency term is based on the diffusion tensor  $x_{DT}$ , the encoding matrix for the  
 142 diffusion tensor representation  $A_{DTI}$ , and the log-transformed signal data  $y$ . The  $n$ 'th row of  $A_{DTI}$   
 143 is given by:  $A_{DTI,n} = (1, -b_{xx,n}, -b_{yy,n}, -b_{zz,n}, -2b_{xy,n}, -2b_{xz,n}, -2b_{yz,n})$   
 144 where  $n$  counts the diffusion directions acquired, and for the  $m$ 'th voxel,  $x_{DT,m} =$   
 145  $(\log(S_{0,m}), D_{xx,m}, D_{yy,m}, D_{zz,m}, D_{xy,m}, D_{xz,m}, D_{yz,m})$ , where  $D_{ij}$  are components of the  
 146 symmetric diffusion tensor (i.e.,  $x_{DT}$  is a vector of length  $7N$ , where  $N$  is the total number of  
 147 voxels). For each voxel position  $m$ , the operator  $T_{DT,m}$  performs a numerical derivative,  $d_i$ ,  
 148 along each of the three spatial dimensions, for each diffusion tensor component:

$$T_{DT,m}x_{DT,m} = (w_{xx}d_xD_{xx,m}, w_{xx}d_yD_{xx,m}, w_{xx}d_zD_{xx,m}, w_{yy}d_xD_{yy,m}, \dots, w_{yz}d_zD_{yz,m}) \quad (9)$$

149 where  $w_{ij}$  is a constant that scales results. For all cases here,  $w_{xx} = w_{yy} = w_{zz} = 1$  and  $w_{xy} =$   
 150  $w_{xz} = w_{yz} = 2$  to account for diffusion tensor cross terms typically having smaller magnitudes

151 than the diagonal of the tensor. The total size of  $T_{DT}x_{DT}$  is 18N, which corresponds to three  
 152 derivatives for each of the six unique elements of the diffusion tensor.

153 *Step Two:* In the second step, we regularize the axisymmetric DKI fitting for the purpose of  
 154 controlling noise amplification in parameter maps using:

$$\operatorname{argmin} \|A_{DKI}x_{DK} - y\|_2^2 + \gamma_{DK} \|T_{DK}x_{DK}\|_2^2 \quad (10)$$

155 where  $x_{DK}$  are the diffusion kurtosis parameters,  $A_{DKI}$  is the encoding matrix for the  
 156 axisymmetric DKI model, and  $\gamma_{DK}$  is the regularization weighting for this step. The  $n$ 'th row of  
 157  $A_{DKI}$  is given by (Eq. 2):

$$A_{DKI,n} = \begin{pmatrix} 1, -b_n(1 - \cos^2\theta_n), -b_n(\cos^2\theta_n), \frac{b_n^2}{6} \left( \frac{10}{16} \cos(4\theta_n) - \frac{8}{16} \cos(2\theta_n) - \frac{2}{16} \right), \\ \frac{b_n^2}{6} \left( \frac{5}{16} \cos(4\theta_n) + \frac{8}{16} \cos(2\theta_n) + \frac{3}{16} \right), \frac{b_n^2}{6} \left( \frac{-15}{16} \cos(4\theta_n) + \frac{15}{16} \right) \end{pmatrix} \quad (11)$$

158 where  $\theta_n$  is determined from the dot product of the diffusion encoding vector with the  
 159 symmetric axis of diffusion within each voxel (primary eigenvector of the fitted diffusion tensor  
 160 from step one), and for the  $m$ 'th voxel,  $x_{DK,m} =$   
 161  $(\log(S_{0,m}), D_{\perp,m}, D_{\parallel,m}, \bar{D}^2 W_{\perp,m}, \bar{D}^2 W_{\parallel,m}, \bar{D}^2 \bar{W}_m)$ . Similar to step one, the operator  $T_{DK,m}$   
 162 performs a numerical derivative in every voxel along each of the three spatial dimensions, for  
 163 each diffusion parameter in  $x_{DK,m}$ :

$$T_{DK,m}x_{DK,m} = \left( d_x D_{\perp,m}, d_y D_{\perp,m}, d_z D_{\perp,m}, d_x D_{\parallel,m}, \dots, d_z \bar{D}^2 \bar{W}_m \right) \quad (12)$$

164 which has a total size of 15N. Units of  $\text{ms}/\mu\text{m}^2$  are used for b-values in all calculations to ensure  
 165 that all the entries of  $T_{DK,m}x_{DK,m}$  are of comparable magnitude to each other since typically  $b \sim$   
 166  $1 \text{ ms}/\mu\text{m}^2$ .

167 A ‘base regularization’ (mouse data:  $\gamma_{DT} = 0.5$ ,  $\gamma_{DK} = 0.075$ , human data:  $\gamma_{DT} = 0.5$ ,  $\gamma_{DK} =$   
168 0.2) was heuristically chosen such that regularization at both steps contributed to the reduction  
169 of noise in subsequent parameter maps while avoiding over-regularization. To investigate the  
170 effect of varying the net regularization, the base regularization weightings were multiplied by a  
171 single factor.

172 Our implementation of axisymmetric fitting with optional spatial regularization is available in  
173 the MatMRI toolbox at <https://gitlab.com/cfmm/matlab/matmri> (Baron, 2021; Varela -  
174 Mattatall et al., 2023).

## 2.5. Data Analysis

### 2.5.1. Comparing kurtosis tensor vs. axisymmetric DKI fitting

175 The DIPY project (Henriques et al., 2021) was used to compute kurtosis metrics via kurtosis  
176 tensor fitting to compare with the axisymmetric fitting method. Ordinary least squares was  
177 used for fitting the kurtosis tensor and metrics were computed using the analytical solution as  
178 outlined previously (Tabesh et al., 2011). It should be noted that ‘mean kurtosis’,  $\bar{W}$ , calculated  
179 using axisymmetric fitting is equivalent to the ‘mean kurtosis tensor’ metric calculated when  
180 fitting the full kurtosis tensor. When reducing the number of diffusion directions for both fitting  
181 methods in HCP data, the reduced direction set that was most uniformly distributed along a  
182 sphere based on electrostatic repulsion was selected (Jones et al., 1999). It should be noted  
183 that the 10 directions used for the HCP data are not the same as the scheme outlined in Table  
184 1. All b=0 images were used when the number of directions was reduced.

### 2.5.2. Variation of principal eigenvector with frequency

185 To determine the validity of using data from all OGSE frequencies to fit the diffusion tensor for  
186 the purpose of finding the symmetric diffusion axis, the variation of principal eigenvector with  
187 frequency was examined. A mask was manually drawn around the brain and the central angle

188 between the 3-dimensional principal eigenvectors was found via the great-circle distance  
189 between them.

### 2.5.3. Methods to calculate the symmetric axis of diffusion

190 We hypothesize that the symmetric axis of diffusion depends negligibly on b-value and OGSE  
191 frequency and, accordingly, it would be most robust to include data from all frequencies and b-  
192 values together when computing the axis of symmetry. To test this hypothesis, maps were  
193 computed with three different ways of determining the symmetric axis: (1) AFAB – Using data  
194 from all frequencies and all b-values to compute a single diffusion tensor in each voxel, with  
195 data from each frequency using the same symmetric axis for parameter fitting. (2) SFAB – Using  
196 data from all b-values to compute a diffusion tensor in each voxel for each frequency  
197 separately, with parameter fitting for each frequency using a different symmetric axis within  
198 each voxel (i.e., the entire fitting process is done independently for each frequency). (3) SFLB –  
199 Using data from only the low b-value shell ( $1000 \text{ s/mm}^2$ ) to compute a diffusion tensor in each  
200 voxel for each frequency separately, with subsequent parameter fitting for each frequency  
201 using data from all b-values.

202 To quantitatively compare these three approaches, region-of-interest (ROI) measurements  
203 were performed in the corpus callosum and hippocampus in mice. ROI masks were generated  
204 from the Turone Mouse Brain Atlas (Klein et al., 2009). First, the atlas was registered to a single  
205 ‘chosen T2’ volume from one of the scanning sessions using affine and symmetric  
206 diffeomorphic transforms with ANTs software (Avants et al., 2011). Similarly, the ‘chosen T2’  
207 volume was registered into each subject’s dMRI native space. The outputted deformation fields  
208 and affine transforms were then used to bring both ROIs into the native space of each subject.  
209 Masks were visually inspected to ensure good registration quality.

#### 2.5.4. Comparing spatial regularization vs Gaussian smoothing

210 To qualitatively compare noise levels in kurtosis maps using Gaussian smoothing and our spatial  
211 regularization algorithm, we chose to use  $K_{\perp}$  maps as they showed the best contrast between  
212 grey and white matter. We implemented our regularization algorithm (during fitting) and  
213 Gaussian smoothing (prior to fitting) on diffusion-weighted images at various strengths which  
214 were chosen so that at each level both maps had an approximately equal visual appearance of  
215 noisy voxels. Comparisons between both methods were assessed qualitatively in both humans  
216 and mice and quantitatively in mice using the ROI analysis procedure outlined above.

### **3. Results**

#### *3.1. Conventional kurtosis tensor vs. axisymmetric DKI fitting*

217 Figure 1 shows human data comparing the two fitting methods at varying numbers of diffusion  
218 directions, with no spatial regularization (i.e.,  $\gamma_{DT} = \gamma_{DK} = 0$ ). Both methods provide  
219 qualitatively similar maps, although maps computed using kurtosis tensor fitting have more  
220 noise. This noise reduction when using axisymmetric fitting is most apparent in  $K_{\perp}$  maps, which  
221 becomes more discernible when the number of direction is reduced.  $K_{\parallel}$  maps show that  
222 axisymmetric fitting provides maps with higher contrast between white and grey matter  
223 whereas this contrast is difficult to discern when using tensor fitting. With fewer directions, the  
224 grey/white matter contrast becomes even worse for tensor fitting. These same differences are  
225 also evident in Figure 2 which shows mouse data comparing the two fitting methods with a  
226 traditional 40-direction scheme. Additionally, the efficient 10-direction scheme with averaging  
227 produces parameter maps with improved contrast and less noise as compared to maps  
228 acquired with more encoding directions, which show over-estimation of kurtosis parameters  
229 and noisy  $\bar{D}$  and FA towards the bottom of the brain where there is low signal-to-noise ratio  
230 (SNR).

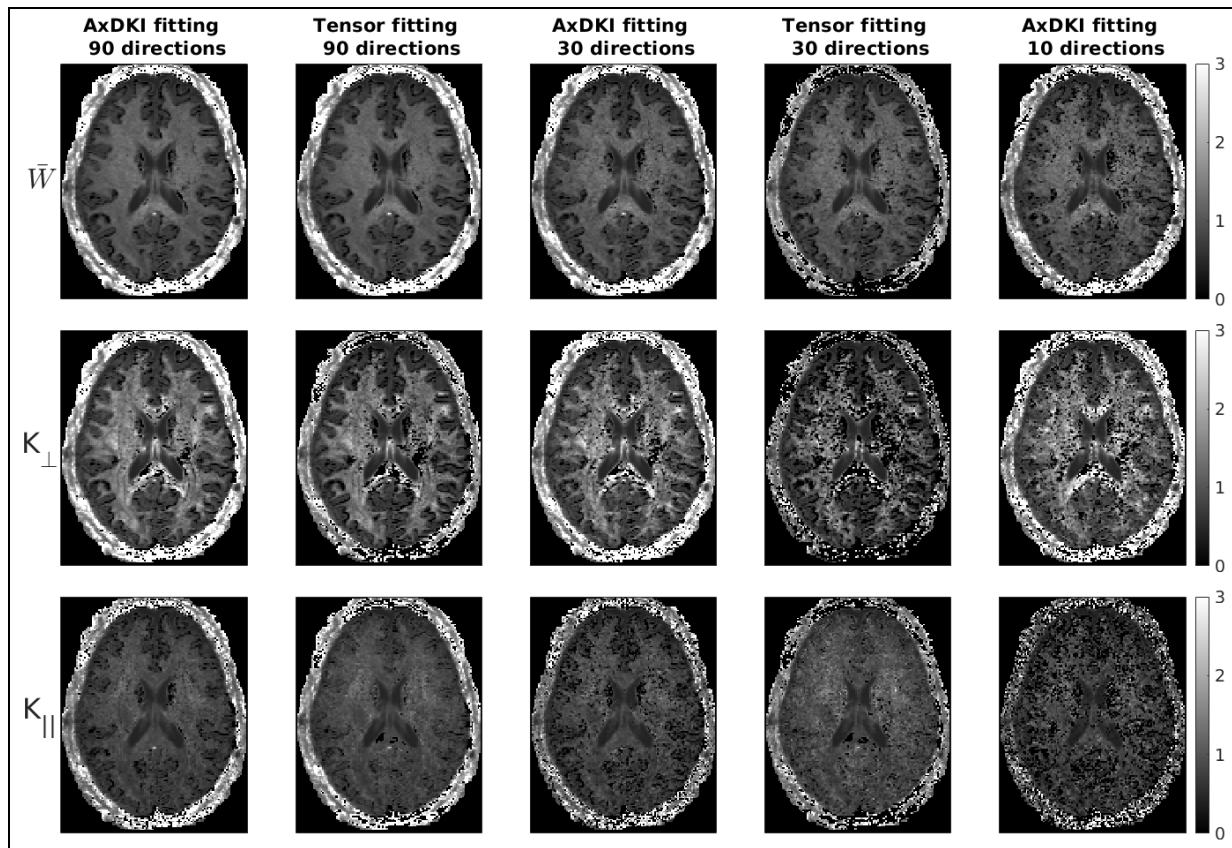


**Figure 1.** Comparison of kurtosis maps when using conventional kurtosis tensor fitting vs axisymmetric DKI (AxDKI) fitting at various numbers of diffusion directions. It should be noted that data shown with 10 directions is not the same scheme as outlined in Table 1.

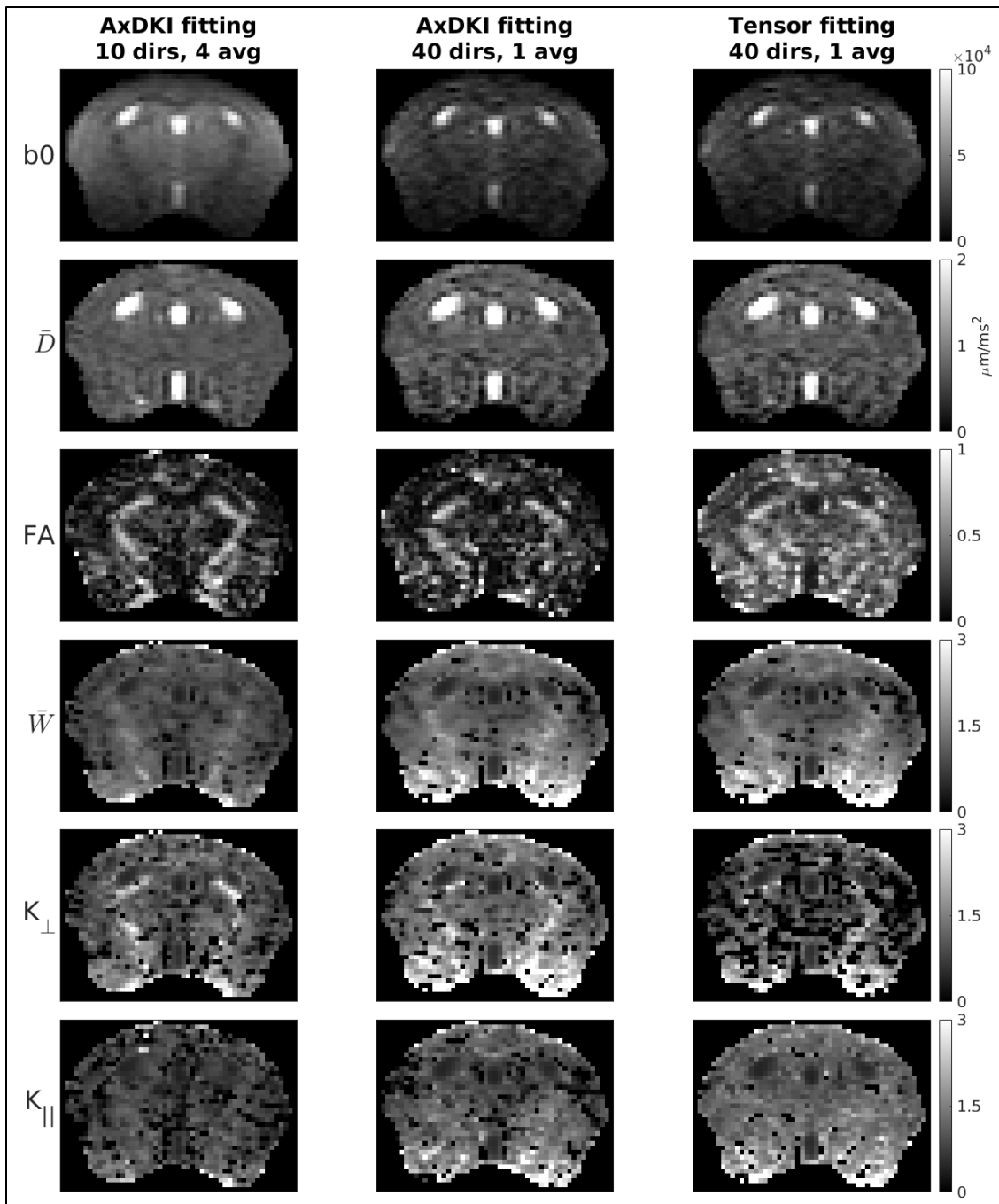


**Figure 2.** Comparison of  $b=0$  images, and diffusion tensor and kurtosis parameter maps computed with the 10-direction scheme with averaging with a traditional 40-direction scheme using axisymmetric DKI (AxDKI) fitting, and axisymmetric fitting vs kurtosis tensor fitting with the 40-direction scheme in a mouse. Data shown is from the PGSE (i.e., 0 Hz) acquisition.

### *3.2. Variation of principal direction of diffusion with frequency*

231 Figure 3a) shows a histogram of the agreement of the principal eigenvector across examined  
232 frequencies when using data from all b-value shells for computation. Good agreement across  
233 frequencies can be seen, with the best agreement being in voxels with high FA values. This can  
234 also be seen qualitatively in Figure 3b), which shows principal diffusion direction maps for each  
235 frequency. Differences between frequencies are difficult to discern qualitatively, especially in  
236 white matter regions. Supplementary Figure 1 shows similar histograms and maps but  
237 demonstrates how this agreement changes when using data from only the low b-value shell  
238 ( $1000 \text{ s/mm}^2$ ) to calculate the diffusion tensor. The distribution shown in the histogram is more  
239 skewed away from collinearity and it is also qualitatively apparent in the principal diffusion  
240 direction maps that the principal eigenvector shows noise-like inconsistencies across  
241 frequencies.



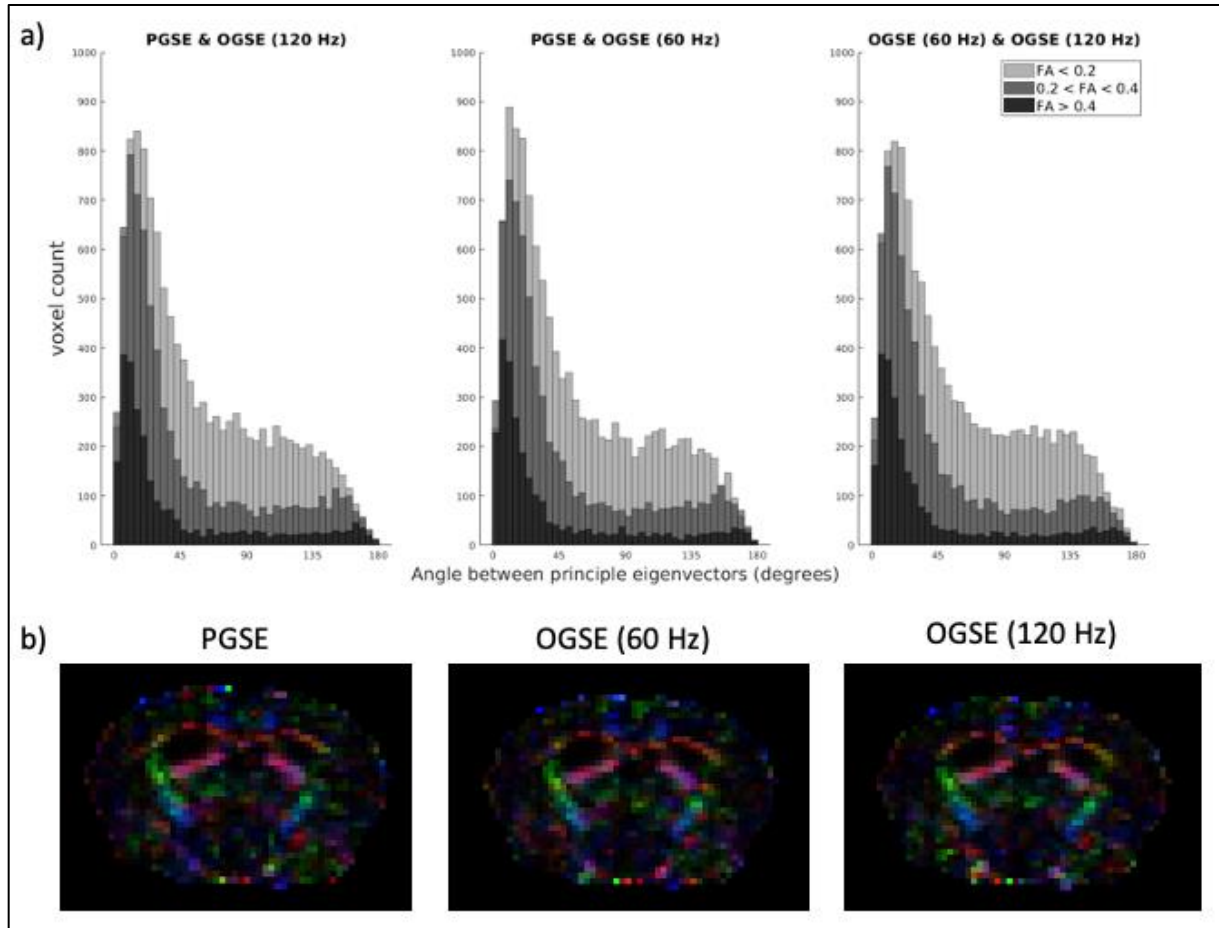


**Figure 3.** Examining the consistency of principal diffusion direction across PGSE and OGSE frequencies when using all  $b$ -value shells to calculate the diffusion tensor. a) shows histograms which quantify the central angle between principal eigenvectors computed at each frequency. b) shows principal diffusion direction maps for the corresponding acquisition above.

### 3.3. Comparing methods to calculate the symmetric axis of diffusion

242 Figure 4 shows kurtosis and FA maps computed when using differing amounts of data to  
 243 calculate the symmetric axis of diffusion via Eq. 8 with no regularization (i.e.,  $\gamma_{DT} = 0$ ).  $\overline{W}$  maps  
 244 appear qualitatively indistinguishable regardless of the method used to calculate the axis of  
 245 symmetry.  $K_{\perp}$  maps appear the least noisy when using data from AFAB to calculate the axis of  
 246 symmetry, with quality degradation being most evident when using data from only the low  $b$ -  
 247 value shell (SFLB) to designate the symmetric axis.  $K_{\parallel}$  maps have an increased noise presence

248 when not using data from all frequencies to determine the symmetric axis, and minimal  
 249 contrast when using data from SFLB. FA maps also show the best image quality when using data  
 250 from all frequencies and b-values to designate the symmetric axis.

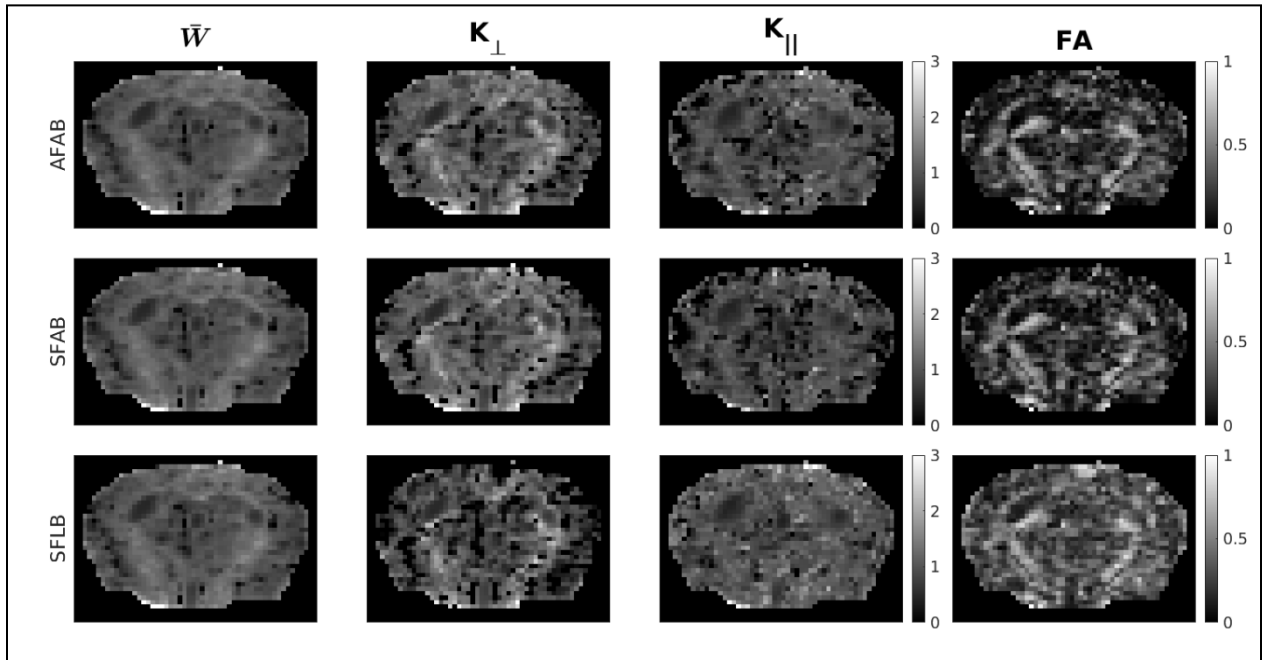


**Figure 4.** Comparison of kurtosis and FA maps when using various methods to calculate the diffusion tensor for axis of symmetry designation with no regularization (AFAB – using data from all frequencies and b-value shells, SFAB – using data from separate frequencies and all b-value shells, SFLB – using data from separate frequencies and only the low b-value shell). Data shown is from the PGSE (i.e., 0 Hz) acquisition.

251 Figure 5 shows quantitative data when using different methods to calculate the axis of  
 252 symmetry in the corpus callosum and hippocampus of a single mouse. As seen in Figure 4,  $\bar{W}$   
 253 appears to be invariant to the axis of symmetry designation. Inclusion of some or all  
 254 frequencies for diffusion tensor estimation resulted in similar quantitative values, with slightly  
 255 decreased  $K_{\parallel}$  when using data from SFAB. Importantly, the frequency dispersion of all kurtosis  
 256 metrics remained relatively consistent no matter the method to calculate axis of symmetry.  
 257 Similar results were observed in other subjects.

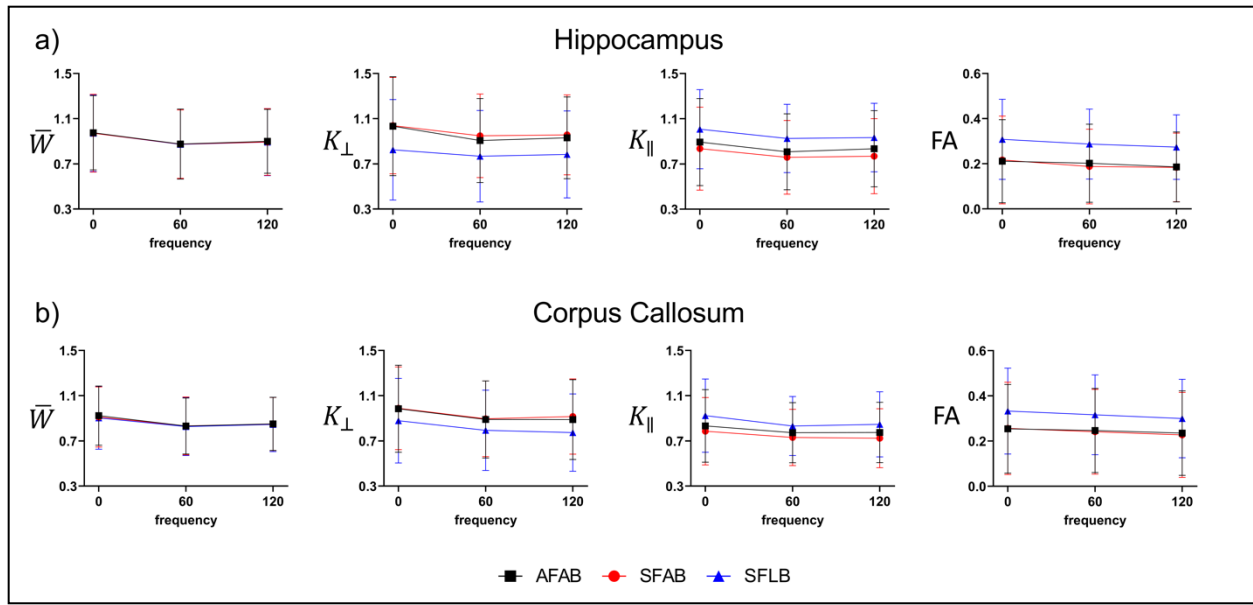


**Figure 5.** Quantitative data on how collapsing data from all frequencies and using all or only the low  $b$ -value shell to compute the axis of symmetry impacts kurtosis and FA values in a representative mouse (AFAB – using data from all frequencies and  $b$ -value shells, SFAB – using data from separate frequencies and all  $b$ -value shells, SFLB – using data from separate frequencies and only the low  $b$ -value shell). a) shows data from the hippocampus and b) shows data from the corpus callosum. All data was measured as mean +/- standard deviation within the same subject.

### 3.4. Spatial regularization to control noise amplification

258 Figure 6 shows kurtosis maps in mice with and without regularization. Regularization notably  
 259 reduces the number of noisy voxels in all maps, while there is little-to-no blurring of the original  
 260 contrast. This is especially evident in  $K_{\perp}$  maps where there is high contrast between white and  
 261 grey matter, which is conserved with regularization.

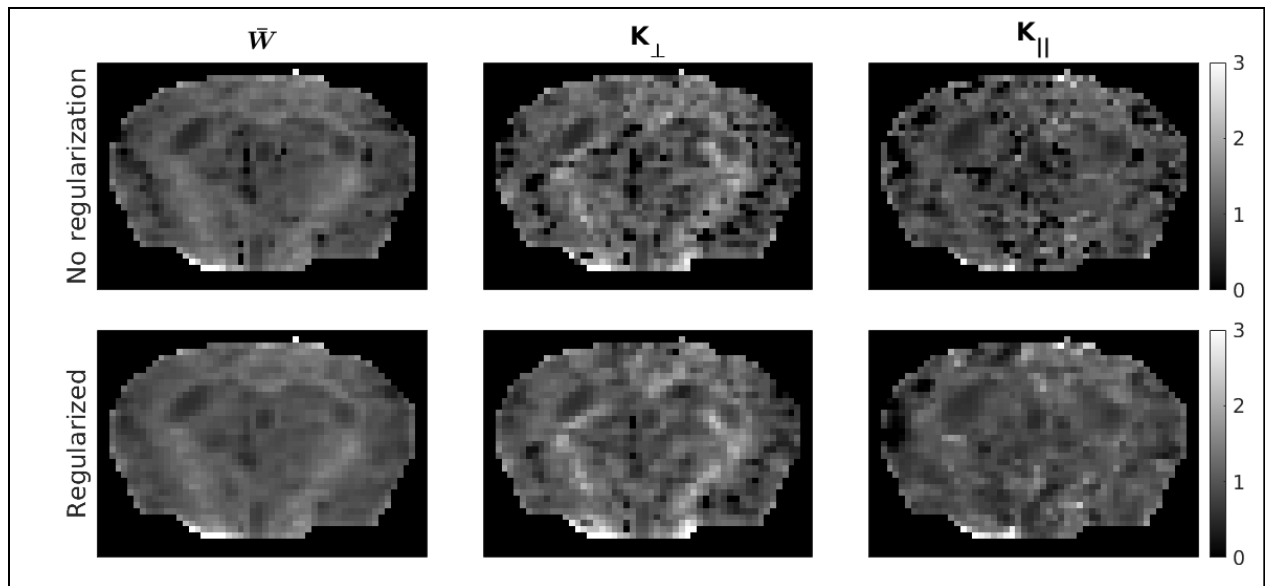


**Figure 6.** Comparison of kurtosis maps with and without implementation of our two-step regularization algorithm. The top row shows unregularized data and the bottom row shows data that produced high quality maps while avoiding over-regularization ( $\gamma_{DT} = 1.5, \gamma_{DK} = 0.225$ ). Data shown is from the PGSE (i.e., 0 Hz) acquisition.

262 Figure 7 shows a similar comparison of unregularized and regularized kurtosis maps in human  
 263 data with only 10 diffusion directions, with unregularized maps computed using 30 and 90  
 264 directions shown for comparison. Similar to data shown in mice, regularization greatly reduces  
 265 the number of noisy voxels in all maps while retaining original contrast. It is evident that the  
 266 regularized data with only 10 directions produces parameter maps with similar or less noise  
 267 than those acquired with 30 directions, at the expense of slightly reduced contrast at the  
 268 borders between white and grey matter.

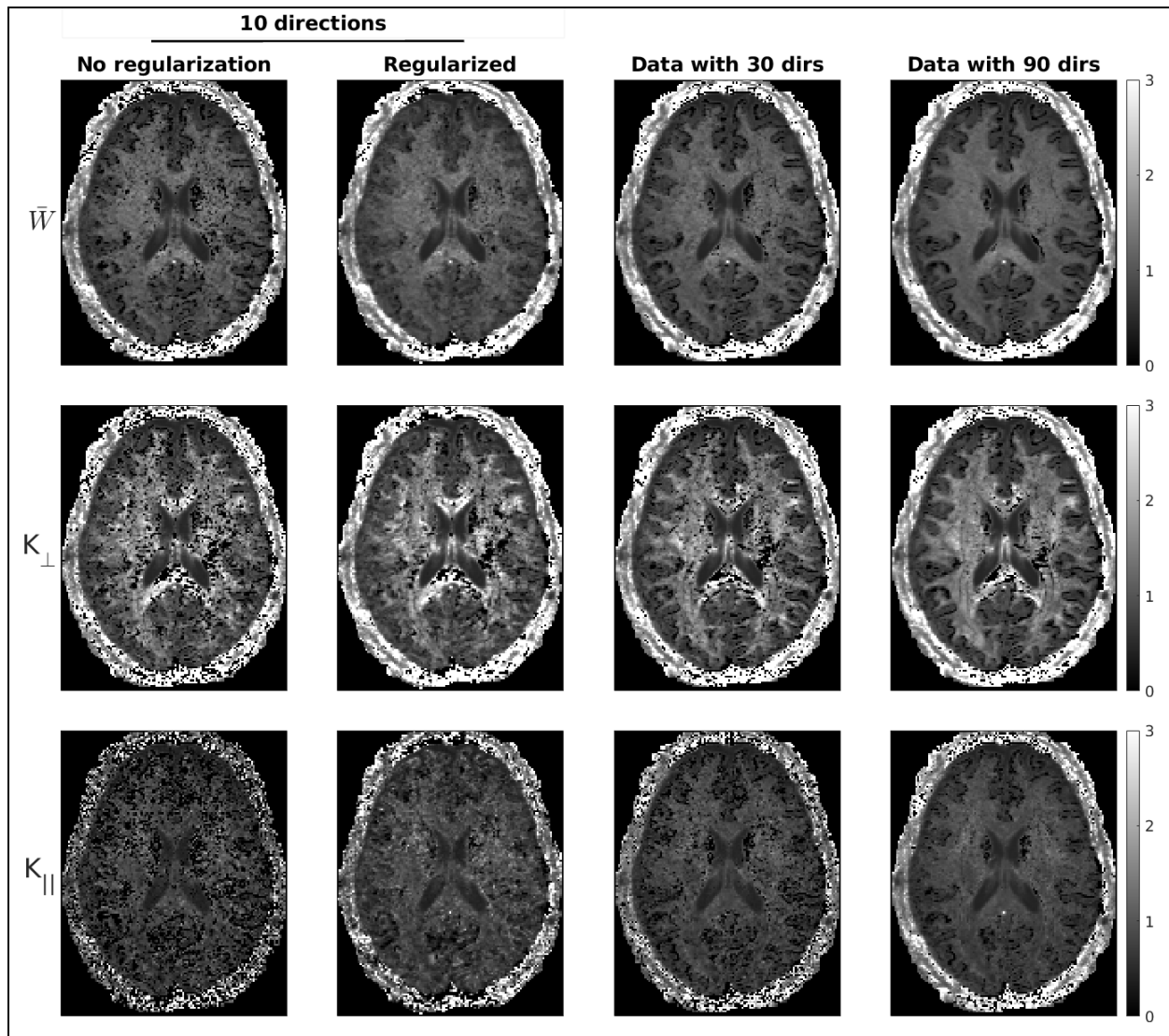


**Figure 7.** Comparison of kurtosis maps with  $(\gamma_{DT} = 1.5, \gamma_{DK} = 0.6)$  and without regularization using 10 diffusion directions, and how regularized maps computed with only 10 directions compare with unregularized data computed using 30 and 90 directions.

269 Figure 8 compares  $K_{\perp}$  maps from a mouse with increasing levels of spatial regularization and  
 270 Gaussian smoothing. Both methods reduce the number of noisy voxels, however, increasing the  
 271 level of smoothing blurs the maps such that the contrast between white and grey matter  
 272 becomes less apparent. In comparison, as the regularization weighting is increased, the number  
 273 of noisy voxels also decreases but the original contrast is preserved. A similar comparison

274 between regularization and smoothing is shown in human data in Supplementary Figure 2,  
 275 which illustrates the same trends.

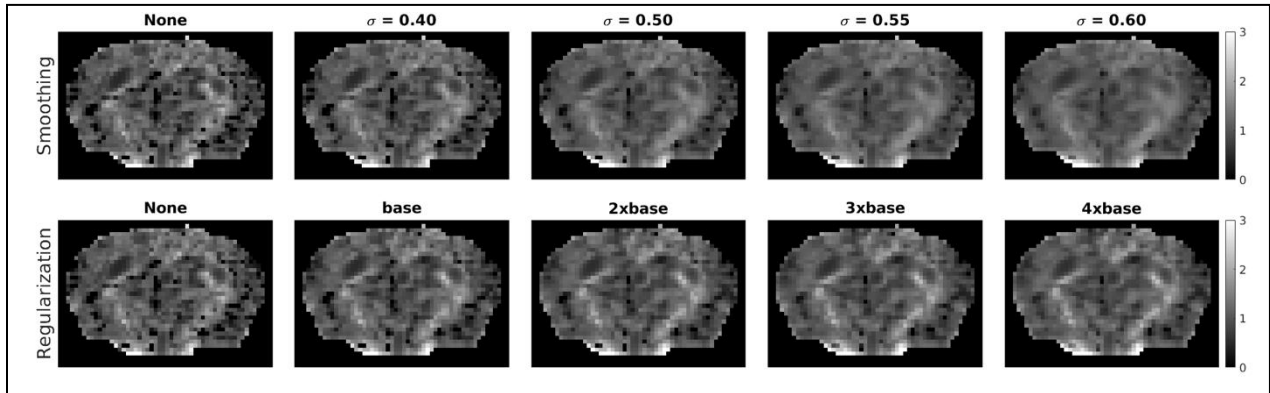


**Figure 8.** Comparison of  $K_{\perp}$  maps with increasing levels of spatial regularization and Gaussian smoothing.  $\sigma$  indicates the standard deviation of the Gaussian kernel used for smoothing on the diffusion-weighted images prior to fitting, in units of voxels. Regularization weighting and  $\sigma$  levels were chosen so that in each column there are approximately equal numbers of noisy voxels in each column. Data shown is from the PGSE (i.e., 0 Hz) acquisition.

276 Figure 9a) and 9b) show how increasing levels of regularization and smoothing impact the inter-  
 277 subject variability of  $\bar{D}$  and kurtosis metrics. It is apparent that with increasing levels of  
 278 regularization the mean value of kurtosis metrics increases, which is expected as the number of  
 279 noisy “blackened” voxels decreases. For Gaussian smoothing there are similar trends, with a  
 280 larger amount of smoothing increasing the mean values in the hippocampus. However, in the  
 281 corpus callosum, the mean value for each kurtosis metric remains consistent with increased  
 282 smoothing while the diffusivity increases. This is likely due to a competing effect whereby noisy  
 283 voxels are being removed, but there is blurring with nearby cerebrospinal fluid which decreases  
 284 the kurtosis and increases diffusivity within white matter. This data also depicts that both  
 285 regularization and Gaussian smoothing have little-to-no effect on the frequency dispersion of  
 286 kurtosis metrics and diffusivity, and the inter-subject variability remains consistent suggesting  
 287 this is due to true variation between subjects.

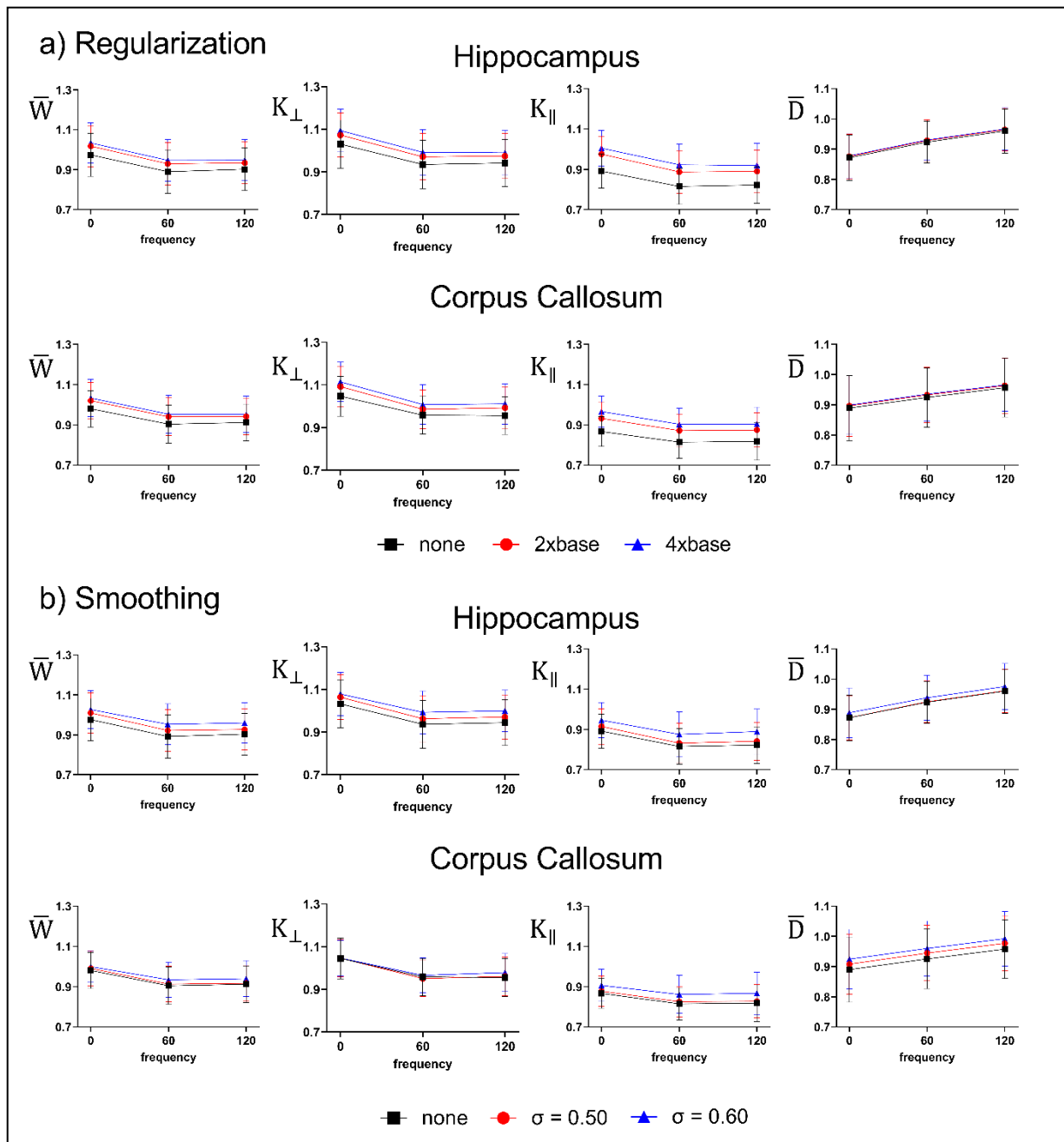


**Figure 9.** Examining how regularization and Gaussian smoothing impacts the inter-subject variability of kurtosis and diffusivity metrics. a) shows how regularization impacts the between subjects ( $n=8$ ) mean and variability within the hippocampus and corpus callosum (base:  $\gamma_{DT} = 0.5, \gamma_{DK} = 0.075$ ). b) shows how smoothing impacts the between subjects mean and variability within each region. Data shown as mean +/- standard deviation across subjects.

#### 4. Discussion

288 In this study, we investigate a method to compute frequency-dependent directional kurtosis  
289 maps, which was used in combination with a 10-direction scheme that has twice the efficiency  
290 of traditional schemes in generating b-value. Axisymmetric DKI fitting was shown to provide  
291 higher quality kurtosis maps as compared to conventional kurtosis tensor fitting, and the 10-  
292 direction scheme with multiple averages was shown to reduce erroneous kurtosis estimation as  
293 compared to traditional schemes with a larger number of directions due to the shorter TE  
294 enabled by the efficient direction scheme. The principal axis of diffusion did not vary  
295 appreciably between the frequencies explored, and we illustrated that using data from all  
296 frequencies and b-values for the purpose of determining the symmetric diffusion axis improved  
297 parameter map quality. Finally, as kurtosis fitting is susceptible to noise amplification, a two-  
298 step spatial regularization algorithm was presented, which reduces noise while preserving  
299 contrast and we showed the advantages of using regularization as opposed to conventional  
300 Gaussian smoothing for controlling noise amplification in DKI maps.

301 Axisymmetric DKI fitting was shown to produce higher quality kurtosis maps as compared to  
302 tensor fitting, becoming more evident when using fewer encoding directions (Figures 1 and 2).  
303 These results agree with two recent simulation studies which found comparable or even slightly  
304 improved performance of axisymmetric DKI compared to tensor fitting in terms of parameter  
305 estimation (Jespersen, 2018; Oeschger et al., 2023). Jespersen (2018) also showed that  
306 axisymmetric DKI generates somewhat more accurate  $K_{\parallel}$  and  $K_{\perp}$  estimation compared to  
307 tensor fitting in cases of low SNR, which agrees with our findings of greater increases in  $K_{\parallel}$  and  
308  $K_{\perp}$  map quality when using axisymmetric DKI with fewer encoding directions. Our finding of  $K_{\parallel}$   
309 contrast being dominated by noise in tensor fitting agrees with Oeschger et al. (2023) who  
310 found axisymmetric DKI is particularly advantageous over tensor fitting in terms of  $K_{\parallel}$   
311 estimation. The improved performance of axisymmetric DKI is likely due to the reduced  
312 parameter space (8 compared to 22) used compared with tensor fitting, which decreases noise  
313 propagation during the fitting process.



314 The challenge in generating large b-values when using oscillating gradient encoding is evident in  
315 both rodent (Aggarwal et al., 2020) and human (Borsos et al., 2023) DKI where tetrahedral  
316 diffusion encoding was required to collect data at 140 Hz in mice and 23 Hz in humans.  
317 Although slightly less efficient in generating b-value, the 10-direction scheme was shown to  
318 generate b-values up to  $\sim 2500$  s/mm<sup>2</sup> at frequencies up to 120 Hz with typical pre-clinical  
319 gradient strengths. While this encoding scheme is not optimized for uniform directional  
320 sampling, the trade-off is a large reduction in TE. Data collected with our efficient 10-direction  
321 scheme achieved a b-value of 2500 s/mm<sup>2</sup> at 120 Hz with a TE of 35.5 ms, while when a 40-  
322 direction scheme was used it required a TE of 52 ms due to the increased diffusion gradient  
323 duration required to achieve the same b-value. Despite the reduced number of encoding  
324 directions compared to a traditional DKI scheme with  $\sim 30$ -40 directions (Fukunaga et al., 2013;  
325 Tabesh et al., 2011), SNR can be recovered by using signal averaging as was done here. We  
326 show in Figure 2 that at the same scan time, an efficient encoding scheme with averaging  
327 produces maps with enhanced contrast in comparison to a higher direction scheme where  
328 there is visible over-estimation of kurtosis metrics in regions with low SNR (Zhang et al., 2021)  
329 (bottom of the brain as we use a surface coil placed on the top of the head) due to the  
330 increased TE. These results compliment the findings by Lebel et al. (2012), which showed that a  
331 6-direction protocol with 5 averages gives comparable robustness in DTI metrics as compared  
332 to a 30-direction protocol even when the greater b-value efficiency of 6 directions is not  
333 exploited and TE's are held constant.

334 The most important step in the axisymmetric fitting method is the determination of a  
335 symmetric diffusion axis in each voxel, which is acquired by fitting the diffusion tensor and  
336 using the primary eigenvector as the symmetric axis. Results showed good agreement of the  
337 primary eigenvector across the frequencies explored (0 to 120 Hz), with the best agreement  
338 occurring in regions with high FA values and when using all b-values for computation (Figure 3  
339 and Supplementary Figure 1). Using frequencies of 0 to 150 Hz, Aggarwal et al. (2012) found  
340 that the primary diffusion direction in voxels with relatively high FA had no apparent frequency-  
341 dependent change. The frequencies explored in this study correspond to hindered-diffusion,

342 specifically average molecular displacements of  $\sim 3.5\text{-}8\ \mu\text{m}$  as determined via the Einstein-  
343 Smoluchowski relation (Morozov et al., 2020). As this displacement range is larger than the  
344 typical diameters of axons in the mouse brain ( $< 1\ \mu\text{m}$ ) (Basu et al., 2023; West et al., 2015), the  
345 water molecules will reach the axonal membrane at all frequencies and therefore the primary  
346 diffusion direction should not vary between frequencies. This is seen as voxels with high FA  
347 values have better agreement between the symmetric axis across frequencies. In grey matter  
348 which is predominated by neuron, astrocyte, and microglia cell bodies with typical diameters of  
349 5-10 microns (Bushong et al., 2002; Kozlowski & Weimer, 2012; Oberheim et al., 2009), it is  
350 possible that the primary diffusion direction could change between the frequencies explored.  
351 Nevertheless, in spherically shaped objects the diffusion tensor eigenvalues are approximately  
352 equal and the primary eigenvector is arbitrary and susceptible to noise.

353 The kurtosis parameter maps presented in Figure 4 show the least amount of noise when using  
354 data from all frequencies and b-values to calculate the symmetric axis of diffusion. This is  
355 expected as the primary diffusion direction is unlikely to change with frequency (as outlined  
356 above) as well as b-value (Tournier et al., 2013), therefore, using data from all frequencies and  
357 b-values will reduce the susceptibility of the diffusion tensor calculation to noise and increase  
358 its robustness. It was shown both qualitatively and quantitatively that  $\bar{W}$  is invariant to the axis  
359 of symmetry designation, whereas  $K_{\perp}$  and  $K_{\parallel}$  map quality is dependent on an accurate  
360 designation of symmetric axis in agreement with previous findings (Hansen et al., 2016).  
361 Importantly, the frequency dispersion of kurtosis metrics remains consistent regardless of the  
362 method used to designate the axis of symmetry.

363 The implementation of the two-step regularization algorithm showed to be advantageous in  
364 reducing noise amplification in kurtosis fitting while preserving contrast in both mice and  
365 humans (Figures 6 and 7). Regularization remains underutilized in dMRI research despite  
366 showing improved image quality in simultaneous multi-slice dMRI data (Haldar et al., 2020),  
367 compressed sensing (Mani et al., 2021; Varela-Mattatall et al., 2023), and estimation of fiber  
368 orientation distribution functions (McGraw et al., 2009; Sakaie & Lowe, 2007). Our results show

369 that regularization is particularly advantageous in improving parameter map quality in DKI,  
370 which are often confounded by noise amplification. Importantly, although this two-step  
371 algorithm was presented for the computation of frequency-dependent kurtosis maps, it can  
372 also be implemented for data acquired at a single diffusion time.

373 While Gaussian smoothing is a widely accepted as a necessary pre-processing step for DKI  
374 (Jensen et al., 2005; Tax et al., 2022), a direct comparison between smoothing and the  
375 proposed regularization implementation was provided, showing improved map quality when  
376 using regularization in both mice and human data (Figure 8 and Supplementary Figure 2). This  
377 aligns with functional MRI research where smoothing was shown to lead to a loss of detail  
378 caused by blurring of activation regions beyond their true boundaries (Liu et al., 2010).  
379 Comparatively, spatial regularization has been shown to improve activity detection and fine  
380 details, given that smoothing introduced via regularization is much less severe than Gaussian  
381 smoothing (Casanova et al., 2009). When comparing the regularized parameter maps to those  
382 obtained with Gaussian smoothing, it is evident that regularization preserves image contrast  
383 much better than smoothing which causes blurring with adjacent structures and cerebrospinal  
384 fluid. Although not explored here, spatial regularization is likely to have advantages over  
385 Gaussian smoothing when conducting voxel-wise analyses, as smoothing can lead to large  
386 distortions in voxels which vary depending on their neighboring voxels. This is because spatial  
387 regularization preferentially smooths the largest errors more strongly (i.e., those with large  
388 spatial gradients), whereas Gaussian smoothing non-specifically smooths all voxels in an image  
389 equally. Finally, we showed that both regularization and Gaussian smoothing have little impact  
390 on the dispersion of kurtosis metrics with frequency and inter-subject variability, which is of  
391 great importance when examining the frequency-dependence of metrics.

392 This study is not without its limitations. As alluded to previously, based on the sizes of  
393 microstructural barriers within tissue, it is not expected that the primary diffusion direction  
394 would change across the frequencies explored in this study. However, this assumption of unity  
395 of the principal diffusion axis across frequencies may not always be true, especially when using

396 very high OGSE frequencies. Although the workflow generates high-quality kurtosis maps in  
397 mice, further investigation of the proposed method should be investigated in humans. Based on  
398 recent work by Dai et al. (2023) who performed frequency-dependent DKI in humans with b-  
399 values of 2000 s/mm<sup>2</sup> and frequencies up to 47.5 Hz with the MAGNUS high performance  
400 gradient system, using the more efficient 10-direction scheme and our fitting algorithm could  
401 allow for increased map robustness and higher b-values and frequencies to be examined in  
402 humans. Additionally, incorporation of spiral trajectories would allow for increased b-value for  
403 a given TE as compared to standard Cartesian trajectories (Michael et al., 2022). Future work  
404 may also explore how different types of regularization (i.e., joint regularization (Bredies et al.,  
405 2010)) can be used to more effectively control noise amplification in kurtosis maps. The  $\ell_2$ -  
406 norm based regularization method was chosen here because it can be evaluated rapidly using  
407 the conjugate gradient method. The computation time was 7 seconds for a full brain mouse  
408 dataset and 64 seconds for human HCP dataset on a workstation with a Intel(R) Core(TM) i9-  
409 11900K (3.5 GHz) and an NVIDIA GeForce RTX 4090 (24 GB). Additionally, the analysis scheme  
410 presented could benefit from automatic selection of the regularization weighting strength  
411 (Varela-Mattatall et al., 2021).

## 5. Conclusions

412 In conclusion, we presented a workflow to generate robust frequency-dependent kurtosis maps  
413 in mice. The 10-direction encoding scheme presented is twice as efficient in generating b-value  
414 compared to traditional schemes, and axisymmetric DKI fitting was shown to provide kurtosis  
415 maps with less noise than conventional tensor fitting and has reduced dataset requirements  
416 that enables fitting with a 10-direction scheme. We showed that using this 10-direction scheme  
417 with multiple averages is advantageous in terms of kurtosis parameter estimation as opposed  
418 to traditional schemes with ~30-40 encoding directions. Furthermore, taking advantage of  
419 degeneracies across frequencies and implementing a two-step regularization algorithm was  
420 shown to decrease noise amplification while maintaining image contrast. While the  
421 interpretation of changes in frequency-dependent kurtosis parameters remain unclear, this  
422 workflow will allow further study of how these changes relate to tissue microstructure and may

423 highlight the frequency-dependence of DKI metrics as useful biomarkers in the study of various  
424 conditions.

## 6. Acknowledgements

The authors would like to thank Amr Eed, Alex Li, and Miranda Bellyou for technical assistance with MRI scans and animal set-up.

This research was supported by the Natural Sciences and Engineering Research Council of Canada: Canada Graduate Scholarships—Master’s Program (NSERC-CGS M), Canada Research Chairs (950-231993), Canada First Research Excellence Fund to BrainsCAN, and the US Department of Defense under congress-directed medical research program (CDMRP), Peer Reviewed Alzheimer’s Research Program (PRARP) by award# W81XWH-20-1-0323.

## 7. Data and code availability statement

Code for our implementation of axisymmetric DKI fitting with optional spatial regularization is available at <https://gitlab.com/cfmm/matlab/matmri>. Human data used in this study is available from the Human Connectome Project at <https://www.humanconnectome.org/study/hcp-young-adult/document/1200-subjects-data-release>, and mouse data is available upon reasonable request.

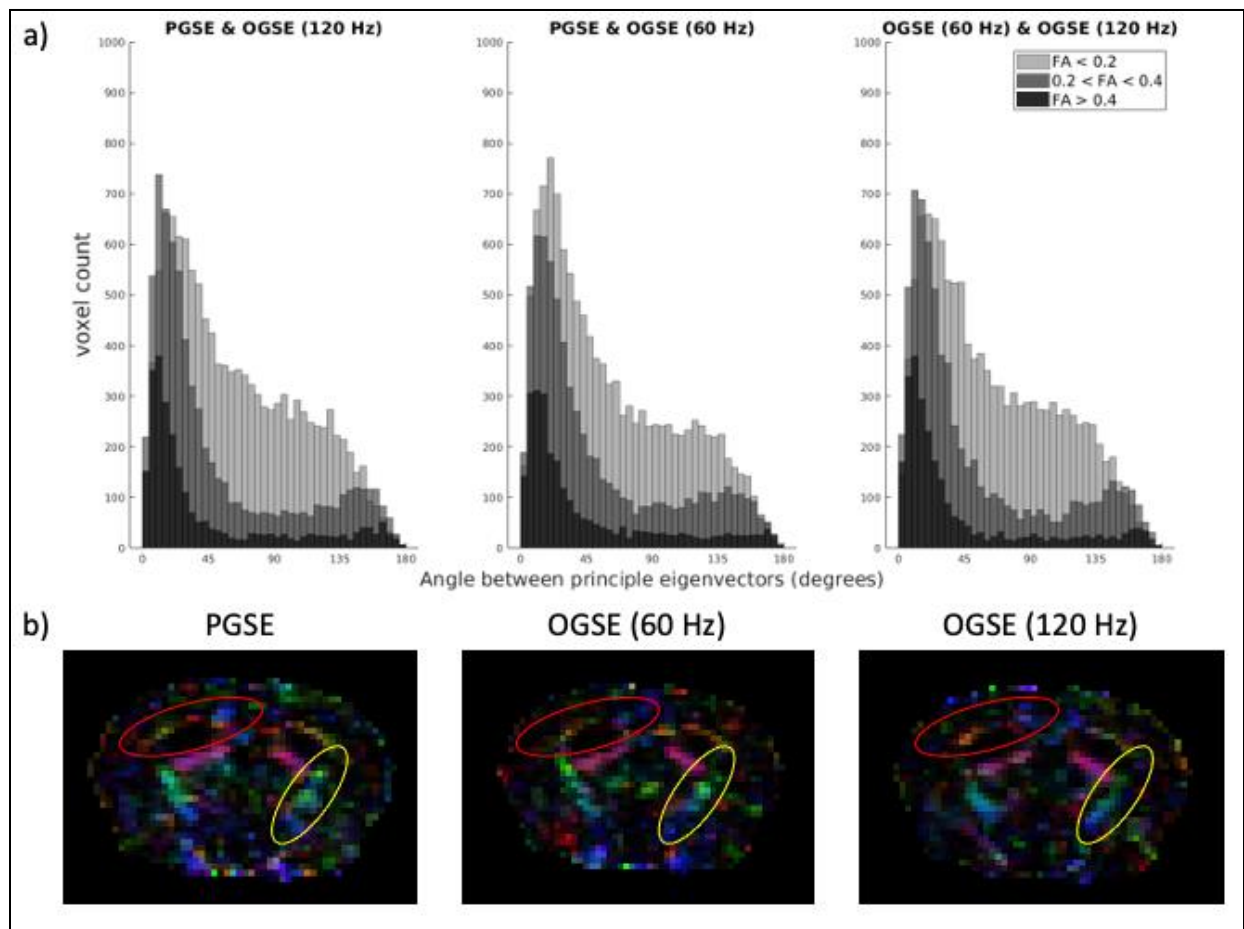
## 8. Author contributions

**Jake Hamilton:** Conceptualization, Data curation, Formal analysis, Investigation, Visualization, Writing – original draft, Writing – review & editing. **Kathy Xu:** Project administration, Resources, Writing – review & editing. **Arthur Brown:** Funding acquisition, Project administration, Resources, Supervision, Writing – review & editing. **Corey A. Baron:** Conceptualization, Funding acquisition, Resources, Software, Supervision, Writing – review & editing.

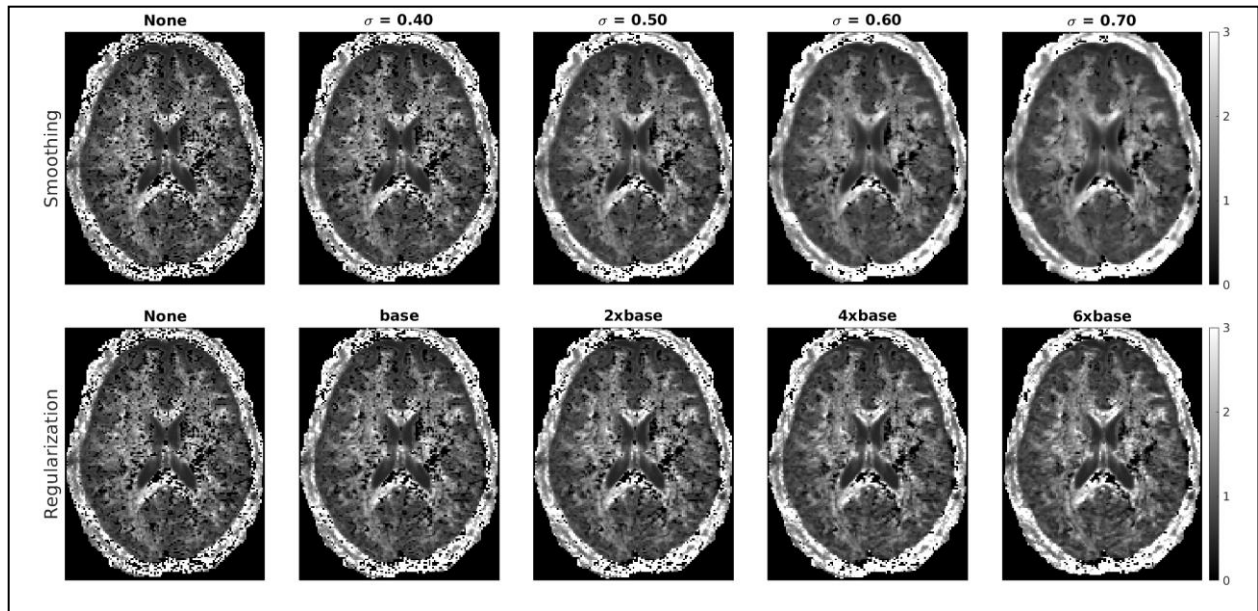
## 9. Declaration of competing interests

The authors declare no competing interests.

## 10. Supplementary Material



**Supplementary Figure 1.** Examining the consistency of principal diffusion direction across PGSE and OGSE frequencies when using only the low  $b$ -value shell to calculate the diffusion tensor. a) shows histograms which quantify the central angle between principal eigenvectors computed at each frequency. b) shows principal diffusion direction maps for the corresponding acquisition above. The corpus callosum is outlined in red and the internal capsule in yellow.



**Supplementary Figure 2.** Comparison of  $K_{\perp}$  maps with increasing levels of spatial regularization and Gaussian smoothing.  $\sigma$  indicates the standard deviation of the Gaussian kernel used for smoothing on the diffusion-weighted images prior to fitting, in units of voxels. Regularization weighting and  $\sigma$  levels were chosen so that in each column there are approximately equal numbers of noisy voxels in each column.

## 11. References

- Aggarwal, M., Burnsed, J., Martin, L. J., Northington, F. J., & Zhang, J. (2014). Imaging neurodegeneration in the mouse hippocampus after neonatal hypoxia-ischemia using oscillating gradient diffusion MRI. *Magnetic Resonance in Medicine*, *72*(3), 829–840. <https://doi.org/10.1002/mrm.24956>
- Aggarwal, M., Jones, M. V., Calabresi, P. A., Mori, S., & Zhang, J. (2012). Probing mouse brain microstructure using oscillating gradient diffusion MRI. *Magnetic Resonance in Medicine*, *67*(1), 98–109. <https://doi.org/10.1002/mrm.22981>
- Aggarwal, M., Smith, M. D., & Calabresi, P. A. (2020). Diffusion-time dependence of diffusional kurtosis in the mouse brain. *Magnetic Resonance in Medicine*, *84*(3), 1564–1578. <https://doi.org/10.1002/mrm.28189>
- Andersson, J. L. R., & Sotiropoulos, S. N. (2016). An integrated approach to correction for off-resonance effects and subject movement in diffusion MR imaging. *NeuroImage*, *125*, 1063–1078. <https://doi.org/10.1016/j.neuroimage.2015.10.019>
- Avants, B. B., Tustison, N. J., Song, G., Cook, P. A., Klein, A., & Gee, J. C. (2011). A reproducible evaluation of ANTs similarity metric performance in brain image registration. *NeuroImage*, *54*(3), 2033–2044. <https://doi.org/10.1016/j.neuroimage.2010.09.025>
- Baron, C. A. (2021). MatMRI: A GPU enabled package for model based MRI image registration (0.1.00). *Zenodo*.
- Baron, C. A., & Beaulieu, C. (2014). Oscillating gradient spin-echo (OGSE) diffusion tensor imaging of the human brain. *Magnetic Resonance in Medicine*, *72*(3), 726–736. <https://doi.org/10.1002/mrm.24987>
- Baron, C. A., Kate, M., Gioia, L., Butcher, K., Emery, D., Budde, M., & Beaulieu, C. (2015). Reduction of Diffusion-Weighted Imaging Contrast of Acute Ischemic Stroke at Short Diffusion Times. *Stroke*, *46*(8), 2136–2141. <https://doi.org/10.1161/STROKEAHA.115.008815>
- Basu, K., Appukuttan, S., Manchanda, R., & Sik, A. (2023). Difference in axon diameter and myelin thickness between excitatory and inhibitory callosally projecting axons in mice. *Cerebral Cortex*, *33*(7), 4101–4115. <https://doi.org/10.1093/cercor/bhac329>



- Borsos, K. B., Tse, D. H. Y., Dubovan, P. I., & Baron, C. A. (2023). Tuned bipolar oscillating gradients for mapping frequency dispersion of diffusion kurtosis in the human brain. *Magnetic Resonance in Medicine*, *89*(2), 756–766. <https://doi.org/10.1002/mrm.29473>
- Bredies, K., Kunisch, K., & Pock, T. (2010). Total Generalized Variation. *SIAM Journal on Imaging Sciences*, *3*(3), 492–526. <https://doi.org/10.1137/090769521>
- Bushong, E. A., Martone, M. E., Jones, Y. Z., & Ellisman, M. H. (2002). Protoplasmic Astrocytes in CA1 Stratum Radiatum Occupy Separate Anatomical Domains. *The Journal of Neuroscience*, *22*(1), 183–192. <https://doi.org/10.1523/JNEUROSCI.22-01-00183.2002>
- Casanova, R., Yang, L., Hairston, W. D., Laurienti, P. J., & Maldjian, J. A. (2009). Evaluating the impact of spatio-temporal smoothness constraints on the BOLD hemodynamic response function estimation: an analysis based on Tikhonov regularization. *Physiological Measurement*, *30*(5), N37–N51. <https://doi.org/10.1088/0967-3334/30/5/N01>
- Chu, X., Wu, P., Yan, H., Chen, X., Fan, L., Wu, Z., Tao, C., Ma, Y., Fu, Y., Guo, Y., Dong, Y., Yang, C., & Ge, Y. (2022). Comparison of brain microstructure alterations on diffusion kurtosis imaging among Alzheimer’s disease, mild cognitive impairment, and cognitively normal individuals. *Frontiers in Aging Neuroscience*, *14*. <https://doi.org/10.3389/fnagi.2022.919143>
- Conklin, C. J., Middleton, D. M., Alizadeh, M., Finsterbusch, J., Raunig, D. L., Faro, S. H., Shah, P., Krisa, L., Sinko, R., Delalic, J. Z., Mulcahey, M. J., & Mohamed, F. B. (2016). Spatially selective 2D RF inner field of view (iFOV) diffusion kurtosis imaging (DKI) of the pediatric spinal cord. *NeuroImage: Clinical*, *11*, 61–67. <https://doi.org/10.1016/j.nicl.2016.01.009>
- Conturo, T. E., Lori, N. F., Cull, T. S., Akbudak, E., Snyder, A. Z., Shimony, J. S., McKinstry, R. C., Burton, H., & Raichle, M. E. (1999). Tracking neuronal fiber pathways in the living human brain. *Proceedings of the National Academy of Sciences*, *96*(18), 10422–10427. <https://doi.org/10.1073/pnas.96.18.10422>
- Dai, E., Zhu, A., Yang, G. K., Quah, K., Tan, E. T., Fiveland, E., Foo, T. K. F., & McNab, J. A. (2023). Frequency-dependent diffusion kurtosis imaging in the human brain using an oscillating gradient spin echo sequence and a high-performance head-only gradient. *NeuroImage*, *279*, 120328. <https://doi.org/10.1016/j.neuroimage.2023.120328>

- Does, M. D., Parsons, E. C., & Gore, J. C. (2003). Oscillating gradient measurements of water diffusion in normal and globally ischemic rat brain. *Magnetic Resonance in Medicine*, *49*(2), 206–215. <https://doi.org/10.1002/mrm.10385>
- Dong, J. W., Jelescu, I. O., Ades-Aron, B., Novikov, D. S., Friedman, K., Babb, J. S., Osorio, R. S., Galvin, J. E., Shepherd, T. M., & Fieremans, E. (2020). Diffusion MRI biomarkers of white matter microstructure vary nonmonotonically with increasing cerebral amyloid deposition. *Neurobiology of Aging*, *89*, 118–128. <https://doi.org/10.1016/j.neurobiolaging.2020.01.009>
- Falangola, M. F., Jensen, J. H., Tabesh, A., Hu, C., Deardorff, R. L., Babb, J. S., Ferris, S., & Helpert, J. A. (2013). Non-Gaussian diffusion MRI assessment of brain microstructure in mild cognitive impairment and Alzheimer’s disease. *Magnetic Resonance Imaging*, *31*(6), 840–846. <https://doi.org/10.1016/j.mri.2013.02.008>
- Falconer, J. C., & Narayana, P. A. (1997). Cerebrospinal fluid-suppressed high-resolution diffusion imaging of human brain. *Magnetic Resonance in Medicine*, *37*(1), 119–123. <https://doi.org/10.1002/mrm.1910370117>
- Fukunaga, I., Hori, M., Masutani, Y., Hamasaki, N., Sato, S., Suzuki, Y., Kumagai, F., Kosuge, M., Hoshito, H., Kamagata, K., Shimoji, K., Nakanishi, A., Aoki, S., & Senoo, A. (2013). Effects of diffusional kurtosis imaging parameters on diffusion quantification. *Radiological Physics and Technology*, *6*(2), 343–348. <https://doi.org/10.1007/s12194-013-0206-5>
- Ginsburg, T. (1963). The conjugate gradient method. *Numerische Mathematik*, *5*(1), 191–200. <https://doi.org/10.1007/BF01385890>
- Glenn, G. R., Tabesh, A., & Jensen, J. H. (2015). A simple noise correction scheme for diffusional kurtosis imaging. *Magnetic Resonance Imaging*, *33*(1), 124–133. <https://doi.org/10.1016/j.mri.2014.08.028>
- Goryawala, M. Z., Heros, D. O., Komotar, R. J., Sheriff, S., Saraf-Lavi, E., & Maudsley, A. A. (2018). Value of diffusion kurtosis imaging in assessing low-grade gliomas. *Journal of Magnetic Resonance Imaging*, *48*(6), 1551–1558. <https://doi.org/10.1002/jmri.26012>

- Grinberg, F., Ciobanu, L., Farrher, E., & Shah, N. J. (2012). Diffusion kurtosis imaging and log-normal distribution function imaging enhance the visualisation of lesions in animal stroke models. *NMR in Biomedicine*, *25*(11), 1295–1304. <https://doi.org/10.1002/nbm.2802>
- Haldar, J. P., Liu, Y., Liao, C., Fan, Q., & Setsompop, K. (2020). Fast submillimeter diffusion MRI using gSlider-SMS and SNR-enhancing joint reconstruction. *Magnetic Resonance in Medicine*, *84*(2), 762–776. <https://doi.org/10.1002/mrm.28172>
- Hansen, B., Shemesh, N., & Jespersen, S. N. (2016). Fast imaging of mean, axial and radial diffusion kurtosis. *NeuroImage*, *142*, 381–393. <https://doi.org/10.1016/j.neuroimage.2016.08.022>
- Henriques, R. N., Correia, M. M., Marrale, M., Huber, E., Kruper, J., Koudoro, S., Yeatman, J. D., Garyfallidis, E., & Rokem, A. (2021). Diffusional Kurtosis Imaging in the Diffusion Imaging in Python Project. *Frontiers in Human Neuroscience*, *15*. <https://doi.org/10.3389/fnhum.2021.675433>
- lima, M., Yamamoto, A., Kataoka, M., Yamada, Y., Omori, K., Feiweier, T., & Togashi, K. (2019). Time-dependent diffusion MRI to distinguish malignant from benign head and neck tumors. *Journal of Magnetic Resonance Imaging*, *50*(1), 88–95. <https://doi.org/10.1002/jmri.26578>
- Jelescu, I. O., Grussu, F., Ianus, A., Hansen, B., Barrett, R. L. C., Aggarwal, M., Michielse, S., Nasrallah, F., Syeda, W., Wang, N., Veraart, J., Roebroek, A., Bagdasarian, A. F., Eichner, C., Sepehrband, F., Zimmermann, J., Soustelle, L., Bowman, C., Tandler, B. C., ... Schilling, K. G. (2022). *Recommendations and guidelines from the ISMRM Diffusion Study Group for preclinical diffusion MRI: Part 1 -- In vivo small-animal imaging*.
- Jensen, J. H., & Helpert, J. A. (2010). MRI quantification of non-Gaussian water diffusion by kurtosis analysis. *NMR in Biomedicine*, *23*(7), 698–710. <https://doi.org/10.1002/nbm.1518>
- Jensen, J. H., Helpert, J. A., Ramani, A., Lu, H., & Kaczynski, K. (2005). Diffusional kurtosis imaging: The quantification of non-gaussian water diffusion by means of magnetic resonance imaging. *Magnetic Resonance in Medicine*, *53*(6), 1432–1440. <https://doi.org/10.1002/mrm.20508>

- Jones, D. K. (2004). The effect of gradient sampling schemes on measures derived from diffusion tensor MRI: A Monte Carlo study. *Magnetic Resonance in Medicine*, *51*(4), 807–815. <https://doi.org/10.1002/mrm.20033>
- Jones, D. K., Horsfield, M. A., & Simmons, A. (1999). Optimal strategies for measuring diffusion in anisotropic systems by magnetic resonance imaging. *Magnetic Resonance in Medicine*, *42*(3), 515–525.
- Kiselev, V. G., & Il'yasov, K. A. (2007). Is the “biexponential diffusion” biexponential? *Magnetic Resonance in Medicine*, *57*(3), 464–469. <https://doi.org/10.1002/mrm.21164>
- Klein, A., Andersson, J., Ardekani, B. A., Ashburner, J., Avants, B., Chiang, M.-C., Christensen, G. E., Collins, D. L., Gee, J., Hellier, P., Song, J. H., Jenkinson, M., Lepage, C., Rueckert, D., Thompson, P., Vercauteren, T., Woods, R. P., Mann, J. J., & Parsey, R. V. (2009). Evaluation of 14 nonlinear deformation algorithms applied to human brain MRI registration. *NeuroImage*, *46*(3), 786–802. <https://doi.org/10.1016/j.neuroimage.2008.12.037>
- Kozlowski, C., & Weimer, R. M. (2012). An Automated Method to Quantify Microglia Morphology and Application to Monitor Activation State Longitudinally In Vivo. *PLoS ONE*, *7*(2), e31814. <https://doi.org/10.1371/journal.pone.0031814>
- Lampinen, B., Lätt, J., Wasselius, J., Westen, D., & Nilsson, M. (2021). Time dependence in diffusion MRI predicts tissue outcome in ischemic stroke patients. *Magnetic Resonance in Medicine*, *86*(2), 754–764. <https://doi.org/10.1002/mrm.28743>
- Lebel, C., Benner, T., & Beaulieu, C. (2012). Six is enough? Comparison of diffusion parameters measured using six or more diffusion-encoding gradient directions with deterministic tractography. *Magnetic Resonance in Medicine*, *68*(2), 474–483. <https://doi.org/10.1002/mrm.23254>
- Liu, W., Zhu, P., Anderson, J. S., Yurgelun-Todd, D., & Fletcher, P. T. (2010). *Spatial Regularization of Functional Connectivity Using High-Dimensional Markov Random Fields* (pp. 363–370). [https://doi.org/10.1007/978-3-642-15745-5\\_45](https://doi.org/10.1007/978-3-642-15745-5_45)
- Lu, H., Jensen, J. H., Ramani, A., & Helpert, J. A. (2006). Three-dimensional characterization of non-gaussian water diffusion in humans using diffusion kurtosis imaging. *NMR in Biomedicine*, *19*(2), 236–247. <https://doi.org/10.1002/nbm.1020>

- Maekawa, T., Hori, M., Murata, K., Feiweier, T., Kamiya, K., Andica, C., Hagiwara, A., Fujita, S., Koshino, S., Akashi, T., Kamagata, K., Wada, A., Abe, O., & Aoki, S. (2020). Differentiation of high-grade and low-grade intra-axial brain tumors by time-dependent diffusion MRI. *Magnetic Resonance Imaging*, *72*, 34–41. <https://doi.org/10.1016/j.mri.2020.06.018>
- Mani, M., Magnotta, V. A., & Jacob, M. (2021). qModel: A plug-and-play model-based reconstruction for highly accelerated multi-shot diffusion MRI using learned priors. *Magnetic Resonance in Medicine*, *86*(2), 835–851. <https://doi.org/10.1002/mrm.28756>
- McGraw, T., Vemuri, B., Özarlan, E., Chen, Y., & Mareci, T. (2009). Variational denoising of diffusion weighted MRI. *Inverse Problems & Imaging*, *3*(4), 625–648. <https://doi.org/10.3934/ipi.2009.3.625>
- McNab, J. A., Edlow, B. L., Witzel, T., Huang, S. Y., Bhat, H., Heberlein, K., Feiweier, T., Liu, K., Keil, B., Cohen-Adad, J., Tisdall, M. D., Folkerth, R. D., Kinney, H. C., & Wald, L. L. (2013). The Human Connectome Project and beyond: Initial applications of 300mT/m gradients. *NeuroImage*, *80*, 234–245. <https://doi.org/10.1016/j.neuroimage.2013.05.074>
- Michael, E. S., Hennel, F., & Pruessmann, K. P. (2022). Evaluating diffusion dispersion across an extended range of b-values and frequencies: Exploiting gap-filled OGSE shapes, strong gradients, and spiral readouts. *Magnetic Resonance in Medicine*, *87*(6), 2710–2723. <https://doi.org/10.1002/mrm.29161>
- Morez, J., Szczepankiewicz, F., den Dekker, A. J., Vanhevel, F., Sijbers, J., & Jeurissen, B. (2023). Optimal experimental design and estimation for q-space trajectory imaging. *Human Brain Mapping*, *44*(4), 1793–1809. <https://doi.org/10.1002/hbm.26175>
- Morozov, S., Sergunova, K., Petraikin, A., Akhmad, E., Kivasev, S., Semenov, D., Blokhin, I., Karpov, I., Vladzimirskyy, A., & Morozov, A. (2020). Diffusion processes modeling in magnetic resonance imaging. *Insights into Imaging*, *11*(1), 60. <https://doi.org/10.1186/s13244-020-00863-w>
- Nilsson, M., Szczepankiewicz, F., Brabec, J., Taylor, M., Westin, C., Golby, A., Westin, D., & Sundgren, P. C. (2020). Tensor-valued diffusion MRI in under 3 minutes: an initial survey of microscopic anisotropy and tissue heterogeneity in intracranial tumors. *Magnetic Resonance in Medicine*, *83*(2), 608–620. <https://doi.org/10.1002/mrm.27959>

- Nørhøj Jespersen, S. (2018). White matter biomarkers from diffusion MRI. *Journal of Magnetic Resonance*, 291, 127–140. <https://doi.org/10.1016/j.jmr.2018.03.001>
- Oberheim, N. A., Takano, T., Han, X., He, W., Lin, J. H. C., Wang, F., Xu, Q., Wyatt, J. D., Pilcher, W., Ojemann, J. G., Ransom, B. R., Goldman, S. A., & Nedergaard, M. (2009). Uniquely Hominid Features of Adult Human Astrocytes. *The Journal of Neuroscience*, 29(10), 3276–3287. <https://doi.org/10.1523/JNEUROSCI.4707-08.2009>
- Oeschger, J. M., Tabelow, K., & Mohammadi, S. (2023). Axisymmetric diffusion kurtosis imaging with Rician bias correction: A simulation study. *Magnetic Resonance in Medicine*, 89(2), 787–799. <https://doi.org/10.1002/mrm.29474>
- Ou, W., & Golland, P. (2005). *From Spatial Regularization to Anatomical Priors in fMRI Analysis* (pp. 88–100). [https://doi.org/10.1007/11505730\\_8](https://doi.org/10.1007/11505730_8)
- Pfefferbaum, A., & Sullivan, E. V. (2003). Increased brain white matter diffusivity in normal adult aging: Relationship to anisotropy and partial voluming. *Magnetic Resonance in Medicine*, 49(5), 953–961. <https://doi.org/10.1002/mrm.10452>
- Portnoy, S., Flint, J. J., Blackband, S. J., & Stanisz, G. J. (2013). Oscillating and pulsed gradient diffusion magnetic resonance microscopy over an extended  $b$ -value range: Implications for the characterization of tissue microstructure. *Magnetic Resonance in Medicine*, 69(4), 1131–1145. <https://doi.org/10.1002/mrm.24325>
- Pyatigorskaya, N., Le Bihan, D., Reynaud, O., & Ciobanu, L. (2014). Relationship between the diffusion time and the diffusion MRI signal observed at 17.2 tesla in the healthy rat brain cortex. *Magnetic Resonance in Medicine*, 72(2), 492–500. <https://doi.org/10.1002/mrm.24921>
- Rahman, N., Xu, K., Omer, M., Budde, M. D., Brown, A., & Baron, C. A. (2021). Test-retest reproducibility of in vivo oscillating gradient and microscopic anisotropy diffusion MRI in mice at 9.4 Tesla. *PLOS ONE*, 16(11), e0255711. <https://doi.org/10.1371/journal.pone.0255711>
- Rudin, L. I., Osher, S., & Fatemi, E. (1992). Nonlinear total variation based noise removal algorithms. *Physica D: Nonlinear Phenomena*, 60(1–4), 259–268. [https://doi.org/10.1016/0167-2789\(92\)90242-F](https://doi.org/10.1016/0167-2789(92)90242-F)

- Sakaie, K. E., & Lowe, M. J. (2007). An objective method for regularization of fiber orientation distributions derived from diffusion-weighted MRI. *NeuroImage*, *34*(1), 169–176. <https://doi.org/10.1016/j.neuroimage.2006.08.034>
- Schachter, M., Does, M. D., Anderson, A. W., & Gore, J. C. (2000). Measurements of Restricted Diffusion Using an Oscillating Gradient Spin-Echo Sequence. *Journal of Magnetic Resonance*, *147*(2), 232–237. <https://doi.org/10.1006/jmre.2000.2203>
- Smith, S. M., Jenkinson, M., Woolrich, M. W., Beckmann, C. F., Behrens, T. E. J., Johansen-Berg, H., Bannister, P. R., De Luca, M., Drobnjak, I., Flitney, D. E., Niazy, R. K., Saunders, J., Vickers, J., Zhang, Y., De Stefano, N., Brady, J. M., & Matthews, P. M. (2004). Advances in functional and structural MR image analysis and implementation as FSL. *NeuroImage*, *23*, S208–S219. <https://doi.org/10.1016/j.neuroimage.2004.07.051>
- Sotiropoulos, S. N., Jbabdi, S., Xu, J., Andersson, J. L., Moeller, S., Auerbach, E. J., Glasser, M. F., Hernandez, M., Sapiro, G., Jenkinson, M., Feinberg, D. A., Yacoub, E., Lenglet, C., Van Essen, D. C., Ugurbil, K., & Behrens, T. E. J. (2013). Advances in diffusion MRI acquisition and processing in the Human Connectome Project. *NeuroImage*, *80*, 125–143. <https://doi.org/10.1016/j.neuroimage.2013.05.057>
- Stenberg, J., Eikenes, L., Moen, K. G., Vik, A., Håberg, A. K., & Skandsen, T. (2021). Acute Diffusion Tensor and Kurtosis Imaging and Outcome following Mild Traumatic Brain Injury. *Journal of Neurotrauma*, *38*(18), 2560–2571. <https://doi.org/10.1089/neu.2021.0074>
- Steven, A. J., Zhuo, J., & Melhem, E. R. (2014). Diffusion Kurtosis Imaging: An Emerging Technique for Evaluating the Microstructural Environment of the Brain. *American Journal of Roentgenology*, *202*(1), W26–W33. <https://doi.org/10.2214/AJR.13.11365>
- Stokum, J. A., Sours, C., Zhuo, J., Kane, R., Shanmuganathan, K., & Gullapalli, R. P. (2015). A longitudinal evaluation of diffusion kurtosis imaging in patients with mild traumatic brain injury. *Brain Injury*, *29*(1), 47–57. <https://doi.org/10.3109/02699052.2014.947628>
- Tabesh, A., Jensen, J. H., Ardekani, B. A., & Helpert, J. A. (2011). Estimation of tensors and tensor-derived measures in diffusional kurtosis imaging. *Magnetic Resonance in Medicine*, *65*(3), 823–836. <https://doi.org/10.1002/mrm.22655>

- Tax, C. M. W., Bastiani, M., Veraart, J., Garyfallidis, E., & Okan Irfanoglu, M. (2022). What's new and what's next in diffusion MRI preprocessing. *NeuroImage*, 249, 118830. <https://doi.org/10.1016/j.neuroimage.2021.118830>
- Tikhonov, A. N., Goncharsky, A. V., Stepanov, V. V., & Yagola, A. G. (1995). *Numerical Methods for the Solution of Ill-Posed Problems*. Springer Netherlands. <https://doi.org/10.1007/978-94-015-8480-7>
- Tournier, J.-D., Calamante, F., & Connelly, A. (2013). Determination of the appropriate *b* value and number of gradient directions for high-angular-resolution diffusion-weighted imaging. *NMR in Biomedicine*, 26(12), 1775–1786. <https://doi.org/10.1002/nbm.3017>
- Tournier, J.-D., Smith, R., Raffelt, D., Tabbara, R., Dhollander, T., Pietsch, M., Christiaens, D., Jeurissen, B., Yeh, C.-H., & Connelly, A. (2019). MRtrix3: A fast, flexible and open software framework for medical image processing and visualisation. *NeuroImage*, 202, 116137. <https://doi.org/10.1016/j.neuroimage.2019.116137>
- Vanhoutte, G., Pereson, S., Delgado y Palacios, R., Guns, P.-J., Asselbergh, B., Veraart, J., Sijbers, J., Verhoye, M., Van Broeckhoven, C., & Van der Linden, A. (2013). Diffusion kurtosis imaging to detect amyloidosis in an APP/PS1 mouse model for Alzheimer's disease. *Magnetic Resonance in Medicine*, 69(4), 1115–1121. <https://doi.org/10.1002/mrm.24680>
- Varela-Mattatall, G., Baron, C. A., & Menon, R. S. (2021). Automatic determination of the regularization weighting for wavelet-based compressed sensing MRI reconstructions. *Magnetic Resonance in Medicine*, 86(3), 1403–1419. <https://doi.org/10.1002/mrm.28812>
- Varela-Mattatall, G., Dubovan, P. I., Santini, T., Gilbert, K. M., Menon, R. S., & Baron, C. A. (2023). Single-shot spiral diffusion-weighted imaging at 7T using expanded encoding with compressed sensing. *Magnetic Resonance in Medicine*, 90(2), 615–623. <https://doi.org/10.1002/mrm.29666>
- Veraart, J., Fieremans, E., Jelescu, I. O., Knoll, F., & Novikov, D. S. (2016). Gibbs ringing in diffusion MRI. *Magnetic Resonance in Medicine*, 76(1), 301–314. <https://doi.org/10.1002/mrm.25866>



- Veraart, J., Novikov, D. S., Christiaens, D., Ades-aron, B., Sijbers, J., & Fieremans, E. (2016). Denoising of diffusion MRI using random matrix theory. *NeuroImage*, *142*, 394–406. <https://doi.org/10.1016/j.neuroimage.2016.08.016>
- Vos, S. B., Jones, D. K., Viergever, M. A., & Leemans, A. (2011). Partial volume effect as a hidden covariate in DTI analyses. *NeuroImage*, *55*(4), 1566–1576. <https://doi.org/10.1016/j.neuroimage.2011.01.048>
- West, K. L., Kelm, N. D., Carson, R. P., & Does, M. D. (2015). Quantitative analysis of mouse corpus callosum from electron microscopy images. *Data in Brief*, *5*, 124–128. <https://doi.org/10.1016/j.dib.2015.08.022>
- Wu, D., Li, Q., Northington, F. J., & Zhang, J. (2018). Oscillating gradient diffusion kurtosis imaging of normal and injured mouse brains. *NMR in Biomedicine*, *31*(6), e3917. <https://doi.org/10.1002/nbm.3917>
- Wu, H., & Yan, S. (2021). Denoising Diffusion MRI via Graph Total Variance in Spatioangular Domain. *Computational and Mathematical Methods in Medicine*, *2021*, 1–8. <https://doi.org/10.1155/2021/4645544>
- Xu, J. (2021). Probing neural tissues at small scales: Recent progress of oscillating gradient spin echo (OGSE) neuroimaging in humans. *Journal of Neuroscience Methods*, *349*, 109024. <https://doi.org/10.1016/j.jneumeth.2020.109024>
- Zhang, Z., Vernekar, D., Qian, W., & Kim, M. (2021). Non-local means based Rician noise filtering for diffusion tensor and kurtosis imaging in human brain and spinal cord. *BMC Medical Imaging*, *21*(1), 16. <https://doi.org/10.1186/s12880-021-00549-9>